Volume 53
Number 4
21 February 2024
Pages 1695–2250

Chem Soc Rev

Chemical Society Reviews

rsc.li/chem-soc-rev

ISSN 0306-0012

ROYAL SOCIETY OF CHEMISTRY

REVIEW ARTICLE

Cuncun Wu, Bo Qu, Lixin Xiao *et al.*

Breaking the bottleneck of lead-free perovskite solar cells through dimensionality modulation

Chem Soc Rev

REVIEW ARTICLE

View Article Online
View Journal | View Issue

Cite this: *Chem. Soc. Rev.*, 2024, **53**, 1769

Breaking the bottleneck of lead-free perovskite solar cells through dimensionality modulation

Wenjin Yu, †[a] Yu Zou, †[a] Hantao Wang,†[a] Siyuan Qi,[a] Cuncun Wu,*[b] Xinyu Guo,[a] Yueli Liu,[a] Zhijian Chen,[a] Bo Qu *[a] and Lixin Xiao *[a]

The emerging perovskite solar cell (PSC) technology has attracted significant attention due to its superior power conversion efficiency (PCE) among the thin-film photovoltaic technologies. However, the toxicity of lead and poor stability of lead halide materials hinder their commercialization. In this case, after a decade of effort, various categories of lead-free perovskites and perovskite-like materials have been developed, including tin halide perovskites, double perovskites, defect-structured perovskites, and rudorffites. However, the performance of the corresponding devices still falls short of expectations, especially their PCE. The limitations mainly originate from either the unstable lattice structure of these materials, which causes the distortion of their octahedra, or their low dimensionality (*e.g.*, structural and electronic dimensionality)-correlated poor carrier transport and self-trapping effect, accelerating nonradiative recombination. Therefore, understanding the relationship between the structures and performance in these emerging candidates and leveraging these insights to design or modify new lead-free perovskites is of great significance. Herein, we review the variety of dimensionalities in different categories of lead-free perovskites and perovskite-like materials and conclude that dimensionality is an important aspect among the crucial indexes that determine the performance of lead-free PSCs. In addition, we summarize the modulation of both structural and electronic dimensionality, and the corresponding enhanced optoelectronic properties in different categories. Finally, perspectives on the future development of lead-free perovskites and perovskite-like materials for photovoltaic applications are provided. We hope that this review will provide researchers with a concise overview of these emerging materials and help them leverage dimensionality to break the bottleneck in photovoltaic applications.

Received 1st September 2023

DOI: 10.1039/d3cs00728f

rsc.li/chem-soc-rev

[a] *State Key Laboratory for Artificial Microstructure and Mesoscopic Physics, Department of Physics, Peking University, Beijing 100871, P. R. China. E-mail: lxxiao@pku.edu.cn, bqu@pku.edu.cn*

[b] *State Key Laboratory of Reliability and Intelligence of Electrical Equipment, School of Materials Science and Engineering, Hebei University of Technology, Tianjin 300130, China. E-mail: cuncunwu@hebut.edu.cn*

† These authors contributed equally to this work.

Wenjin Yu

Wenjin Yu is currently a PhD student at the Department of Physics, Peking University. He received his B.S. Degree in Physics from Peking University in 2018. His interests focus on the chemical mechanism of perovskite crystallization and device physics for both perovskite light-emitting diodes and solar cells.

Yu Zou

Yu Zou is a PhD student at the Department of Physics, Peking University. He received his Bachelor's Degree from Peking University in 2019. His current research focuses on the crystallization mechanism and novel optoelectronic properties of perovskite materials, as well as device optimization for perovskite solar cells and exploration of novel lead-free perovskite materials.

1. Introduction

With the global demand towards a low-carbon society, renewable energy sources such as solar energy have emerged and will soon become an important part of energy systems. The power conversion efficiency (PCE) of perovskite solar cells (PSCs) has risen rapidly to become a leader among the thin-film photovoltaic technologies.[1–7] However, the presence of toxic lead (Pb) ions in efficient PSCs is problematic during their fabrication and application. Also, strict legislation on Pb usage further impedes the widespread adoption of PSCs.[8] Thus, replacing Pb with other less toxic elements has long been a significant and attractive project in the field of PSCs.[9–13] Recent efforts have been devoted to replacing Pb with divalent metals (such as tin(II))[14,15] or combining monovalent and trivalent metals to construct double perovskites.[16,17] In addition, other low-dimensional derivatives such as vacancy-ordered double perovskites (*e.g.*, Cs_2SnI_6 and Cs_2TiBr_6[18,19]), $A_3B_2X_9$ defect structure with two typical polymorphs[20–22] and perovskite-like rudorffites (*e.g.*, Ag_3BiI_6, Ag_2BiI_5, $AgBiI_4$, and $AgBi_2I_7$[23]) have been developed (Fig. 1).

(1) Divalent-metal-based perovskites: due to their ideal bandgap (1.3–1.4 eV) and high carrier mobility, tin(II) halide perovskite solar cells (THPSCs) are associated with a high theoretical efficiency (more than 30%).[24] However, their record PCE remains below 15%, which is much lower than that of Pb PSCs.[25] The main reason for this is the tendency of Sn^{2+} to be oxidized to Sn^{4+}, which is ascribed to the lack of lanthanide contraction, resulting in a relatively smaller effective nuclear charge (Z_{eff}) for the 5s lone-pair electrons than the 6s lone-pair electrons (*i.e.*, Pb^{2+}).[26] Furthermore, the unintended generation of Sn^{4+} in perovskite films results in the formation of high defect densities and inappropriate bandgap (1.7–1.8 eV), and thus poor photovoltaic properties.[27] In addition, homovalent substituents with other divalent metals such as Ge^{2+}, Cu^{2+} and Zn^{2+} suffer from structural instability due to geometrical constraints and energetically favorable distortion.[28]

(2) Double perovskites: although double perovskites (*e.g.*, $Cs_2AgBiBr_6$) or vacancy-ordered double perovskites (*e.g.*, Cs_2SnI_6) are three-dimensional (3D) structures, their key problems are isolated band-edge-deriving octahedra and strong electron–phonon coupling, which hinder the mobility of photo-generated carriers.[29,30] In addition, their relatively large bandgap for single-junction PSCs and indirect bandgap are also detrimental to solar energy harvesting.[31–34]

(3) $A_3B_2X_9$ perovskites: in regard to $A_3B_2X_9$ perovskites, in which the trivalent metal cations Bi and Sb occupy the B-site, two different polymorphs exist, including a zero-dimensional (0D) non-perovskite phase, with indirect bandgaps ranging from 2.1 eV to 2.3 eV, and two-dimensional (2D) layered structure, with double octahedral layers separated by B(III) vacancies.[35] Compared to its 0D counterpart, the 2D polymorph exhibits a direct bandgap of about 2 eV and possesses intrinsic stability at high temperatures and humidity levels.[36] However, the relatively low carrier mobility and large bandgap of $A_3B_2X_9$ PSCs hinder their development.[37,38]

(4) Perovskite-like rudorffites: inspired by superior perovskite compounds, perovskite-derivative-structured materials such as rudorffites may also be highly promising. Unlike the corner-sharing octahedra found in the perovskite structure, the rudorffite structure is characterized by the presence of edge-sharing octahedra, resulting in reduced dimensionality.[39] Although the direct bandgap between 1.79 and 1.83 eV in four compounds (i.e., Ag_3BiI_6, Ag_2BiI_5, $AgBiI_4$ and $AgBi_2I_7$)[23] is suitable for photovoltaic applications, the devices based on

Hantao Wang

Hantao Wang obtained his BS Degree in Microelectronics at Xi'an Jiaotong University in 2021 and is pursuing his PhD in the School of Physics at Peking University, under the supervision of Prof. Lixin Xiao. His current research topic focuses on lead-free perovskite solar cells.

Bo Qu

Bo Qu has been an Associate Professor in the Department of Physics, Peking University since 2013. He received his PhD from Peking University in 2008. He has been working on organic optoelectronics, especially on solar cells and OLEDs.

Lixin Xiao

Lixin Xiao is a Full Professor in the Department of Physics, Peking University. He is an RSC Fellow. He received his PhD from University of Tokyo in 2000. He has been working on optoelectronic devices.

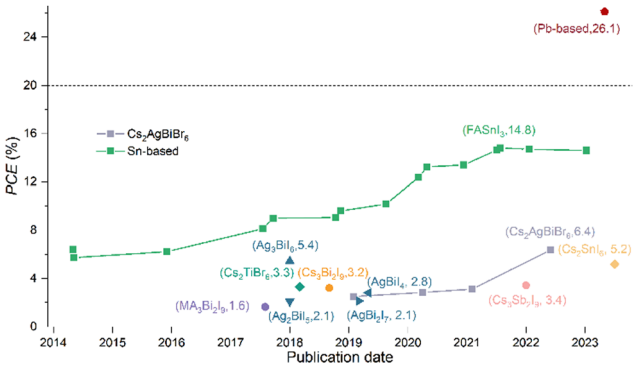

Fig. 1 Timeline of the record PCE among PSCs based on various categories of lead-free perovskites.

these materials still exhibit a disappointing performance owing to their relatively low carrier mobility and severe defect problem.

Dimensionality, including structural and electronic dimensionality, is an important aspect among the crucial indexes that determine the efficiency of lead-free PSCs. Unlike the conventional concept of structural dimensionality, the concept of electronic dimensionality represents the special connectivity of the valence band maximum (VBM) and/or conduction band minimum (CBM), thus possesses more relevance to photovoltaic properties. There is also evidence that dimensionality modulation is a universal strategy for different categories of lead-free perovskites. In this review, we aim to summarize the dimensionality modulated lead-free perovskites, including a thorough review of their structural dimensionality and electronic dimensionality adjustment and the corresponding enhanced optoelectronic properties. The unique adjustment of dimensionality among the various categories can be summarized as follows (Fig. 2):

(1) In THPs, low-dimensional (LD) phases can modulate crystallization to obtain highly crystalline and oriented films with reduced nonradiative recombination, protect 3D phases from oxidation by enhanced chemical stability and dense and hydrophobic surface coverage, and also yield better energy level alignment.

The new design of Ge-based low-dimensional perovskites using intermolecular bonds to scaffold 2D perovskites can inspire new stable low-dimensional perovskites with a small ionic radius metal center for potential application in photovoltaics.

(2) Double perovskites in 2D layered form possess direct bandgaps and can be stable after being iodized for appropriate bandgaps with easily distorted octahedra. Increasing the electronic dimensionality of double perovskites by lattice-ordering modulation or interstitial doping can improve the carrier mobility, inhibit self-trapping effect, and thus increase the carrier diffusion length.

(3) Turning the 0D-dimer conformation into a 2D-layer one in $A_3B_2X_9$ defect-structured perovskites and further increasing the electronic dimensionality significantly enhance the performance of the correlated PSCs.

(4) The flexibility of dimensionality in perovskite-like rudorffites, which significantly affects their characteristics, makes this category designable and diverse.

2. Designing low-dimensional structures for divalent-metal-based perovskites

As the basis for the later discussion on the optimization of PSCs, three main parameters affect the PCE, according to the following equation:

$$\mathrm{PCE} = \frac{J_{\mathrm{SC}} V_{\mathrm{OC}} \mathrm{FF}}{P_{\mathrm{in}}} \quad (1)$$

Obviously, we can enhance the PCE from these three parameters as follows: increasing the short-circuit current density (J_{SC}) by optimizing the bandgap, improving the light harvest

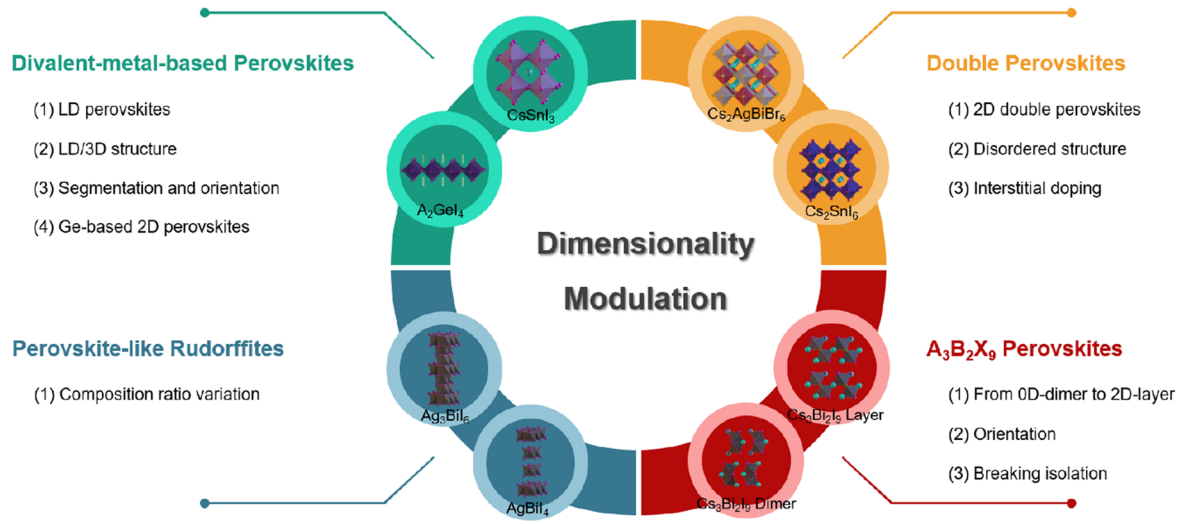

Fig. 2 Schematic illustration of dimensionality modulation in various categories of lead-free perovskites or perovskite-like rudorffites.

efficiency, and increasing the carrier extraction ability; the open-circuit voltage (V_{OC}) by surface passivation and matching the energy-level alignment in devices; and the fill factor (FF) by optimizing the resistance.

2.1 The bottleneck of 3D THPs

Sn has a similar outer electronic configuration (ns^2 np^2) and ionic radius to Pb (Sn^{2+} 1.15 Å and Pb^{2+} 1.19 Å), implying its excellent optical and electrical properties, and thus Sn can be used to partially or completely replace Pb in perovskites with only slight crystal lattice distortion.[40] Due to their ideal bandgap (1.2–1.4 eV), high carrier mobility, low exciton binding energy and strong light absorption coefficient, THPSCs possess the high theoretical efficiency of around 33.4%. The pioneering studies on THPSCs were reported by Snaith and Kanazitdis, achieving the PCE of 6.4% and 5.7%, respectively.[41,42] However, the performance of THPSCs did not realize a significant breakthrough in the following years due to two barriers.[43–45] Firstly, the easy formation of Sn vacancies (V_{Sn}) and Sn^{4+} cations leads to a unipolar p-type characteristic and unfavorable carrier transport, resulting in a low V_{OC} and PCE, as well as poor stability in THPSCs especially in an oxygenated environment (Fig. 3).[46,47] Secondly, SnI_2 undergoes a more rapid reaction with organic ammonium cations such as MAI and FAI due to the higher Lewis acidity from its more active 5s electrons.[48] Furthermore, the rapid and uncontrolled crystallization process of THPs yields poor-quality films with numerous pinholes and defects, resulting in severe nonradiative recombination and leakage current, as well as easy penetration of moisture and oxygen, leading to poor efficiency and stability.

To date, various methods including component engineering, crystallization regulation, antioxidant strategies and structure optimization have been investigated to overcome the above-mentioned limitations. First and foremost, the component engineering of the precursors is essential to reduce the formation of V_{Sn}. The introduction of SnF_2 or $SnCl_2$ in the precursor can enhance the chemical potential of Sn and also the formation energy of V_{Sn} in the perovskite, effectively reducing the generation of V_{Sn}, and thus has become a widely used strategy.[49] The crystallization regulation is mainly focused on slowing down the crystallization rate and promoting the orientation growth to deposit films with high crystallinity, low defect density, and favorable orientation.[43,50–57] Reductive precursors and/or additives can effectively inhibit the rapid oxidation during the crystallization and operation processes, and thus avoid an excessive Sn^{4+} concentration inside the film.[58–63] Also, device structure optimization, such as the choice of p–i–n structure to avoid the accelerated oxidation by the metal oxide electron transport layer (ETL) and facilitate hole extraction, the introduction of a protective layer on the perovskite surface to prevent the penetration of moisture and oxygen, and the optimal choice of transport layers, also contribute to the device efficiency and stability.[64,65]

However, regulation by these external factors still leaves complex problems. Strongly coordinating solvents and additives in crystallization regulation have the potential risk to oxidize Sn^{2+}, while the reductive reagent is constantly consumed during device operation and eventually depleted, leading to the oxidation of the film.[48,66] In addition, these overly complex systems are not conducive to precise control of crystallization and susceptible to unfavorable additive segregation. Also, the large energy level offset between THPs and the commonly used transport materials in Pb-based PSCs results in significant V_{OC} loss. The fundamental reason for these problems is that the basic structure and intrinsic properties of 3D THPs remain after the aforementioned modulations, and the resulting disadvantages cannot be eliminated by simple regulation of external factors.

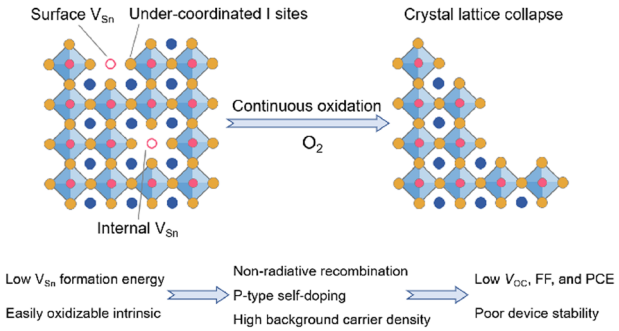

Fig. 3 Schematic illustration of the oxidative degradation processes in THPs.

2.2 Low-dimensional-structured THPs

LD Pb-based perovskites exhibit superior stability to conventional 3D perovskites due to their larger formation energy and the strong hydrophobicity of the large organic spacer cations.[67–70] Also, they result in better energy alignment with the transport layers.[67,68] Inspired by this, LD THPs have been considered to obtain stable and efficient THPSCs, whose general formula can be written as $(A')_m(A)_{n-1}Sn_nX_{3n+1}$, where A′ is the organic spacer cation, A represents methylammonium or formamidine, etc., and n stands for the thickness. Ordinarily, pure 2D perovskites ($n = 1$) with strong quantum and dielectric confinement are unfavorable for photovoltaic applications. Therefore, considering both efficiency and stability, LD THPs always appear in quasi-2D structures ($n > 1$) in most studies.

As shown in Fig. 4, Cao *et al.* and Liao *et al.* developed LD THPSCs with PCEs of 2.5% and 5.9%, respectively, triggering a significant increase in device stability and reproducibility thereafter.[71,72] With a deeper understanding of the nature of LD THPs and the fabrication process optimization, the certified PCE of THPSCs has reached over 14%.[73] Unlike LD Pb-based PSCs, LD THPSCs even have a better performance than that of 3D devices, demonstrating the unique advantages of the LD structure in solving the problems of THPSCs. Based on this, we systematically analyze the unique intrinsic properties of LD THPs and their advantages in THPSCs to break through the bottlenecks mentioned in the previous section. Encouragingly, the construction of LD THPs by dimensionality reduction is expected to solve the major challenges plaguing THPSCs without introducing unfavorable external factors. Furthermore,

we analyze in depth the important factors and possible technology routes from the dimensional modulation perspective to be considered in the specific fabrication of efficient and stable LD THPSCs.

2.2.1 LD/3D structure to improve the efficiency and stability of THPSCs. We specifically analyze the advantages arising from LD THPs based on three perspectives, *i.e.*, high crystalline quality, enhanced stability, and improved energy level alignment.

The poor quality of 3D THPs deposited by conventional methods with rough surfaces, numerous pinholes and grain boundaries leads to undesirable dangling bonds, defects, and leakage current. In addition, the easily generated V_{Sn} may lead to undesirable nonradiative recombination, short carrier diffusion length, ion migration and structural instability, inhibiting the device V_{OC}, FF, PCE and stability. Optimization of the crystallization dynamics by the large amine ligands of LD THPs enables the deposition of high-quality films with fewer grain boundaries, resulting in a significantly lower defect density, ordered and delocalized excitons, longer carrier diffusion length, and less nonradiative recombination.[74] By adjusting the type and ratio of large organic cations, uniform, pinhole-free, smooth, and dense films can be successfully achieved.[72,75] The intermediate phase during crystallization can be further regulated by multi-large cation mixture engineering to direct the highly oriented growth of THPs.[76,77] Diverse methods such as post-treatment,[78] continuous vapor deposition,[79] pre-embedding strategies,[80,81] and spin-coating of LD-3D mixed precursor solutions[45,82] were all used to introduce large organic cations. In addition to inhibiting the formation of Sn^{4+} and V_{Sn}, the electron-rich conjugated portions and amine groups on the large organic cations of 2D THPs can passivate the pre-existing defects.[70,72,82–89] Although some studies did not clarify whether bulky amines form the 2D phase, their effective passivation provides ideas for the subsequent design of other functional large organic cations. Fundamentally, we believe that the strategy of crystallization modulation and passivation by 2D THPs benefits from the stronger interaction ability of 2D spacers compared to their 3D components and leads to the formation of high-quality THP films with reduced defects and ordered orientation.

The mechanism of enhanced stability by the introduction of LD THPs is summarized as Fig. 5. Combining density functional

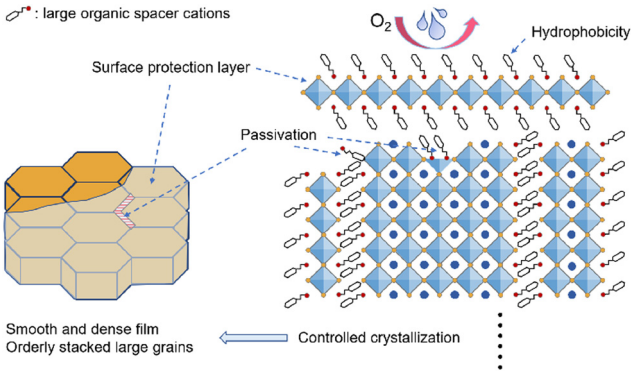

Fig. 5 Mechanism of LD THPs to optimize the overall film stability.

theory (DFT) calculations and specific experiments, several studies have demonstrated that LD THPs have smaller decomposition enthalpies and larger formation energies, and thus higher thermodynamic stability and antioxidant properties.[72] LD-phase-induced high-quality THP films exhibit reduced grain boundaries and defects, resulting in enhanced overall structural and component stability.[85] Meanwhile, the bulky organic spacer cations of LD THPs with strong hydrophobicity and great steric hindrance can effectively block the intrusion of oxygen and moisture from the surface and the grain boundaries.[25,85,88] In addition, unique microstructures such as LD/3D wrapping structure can effectively utilize the advantages of 2D THPs to fully protect the 3D perovskite inside and enhance the device stability under ambient conditions. Liao *et al.* successfully constructed 2D/3D heterojunction THPSCs by introducing FPEABr. The outer 2D THPs existed both on the surface and at the grain boundaries of the 3D $FASnI_3$, effectively wrapped the 3D grains with a reductive atmosphere, and effectively blocked the penetration of moisture and oxygen, resulting in a significantly improved device performance of 14.81% (14.03% certified) and stability. Similarly, full coverage encapsulation by 2D THPs or surface coverage by post-treatment, vapor phase deposition, etc., can effectively retard the surface reactions and prevent the oxidation of Sn^{2+}.[78,79]

Besides, the large energy level offset between 3D THPs and the transport layers leads to severe V_{OC} loss in THPSCs. The introduction of bulky amines and LD THPs can influence the energy level of the active layer and facilitate band alignment with the transport layers.[25,78,85] The better-matched energy level results in rapid carrier extraction and reduced recombination loss at the interface, effectively improving the V_{OC} and PCE. The direction of the energy band shift will change when the introduced large organic cations do not form 2D THPs, or when the original precursor system is already of mixed dimensions or other complex compositions.[88,90,91]

In summary, to break the bottleneck of 3D THPSCs, the introduction of LD THPs effectively improves the intrinsic stability and resistance of the films to moisture and oxygen. Meanwhile, the high-quality films with fewer defects and ordered crystallites, as well as favorable energy level alignment facilitate the carrier transport and extraction inside the devices (Fig. 6).

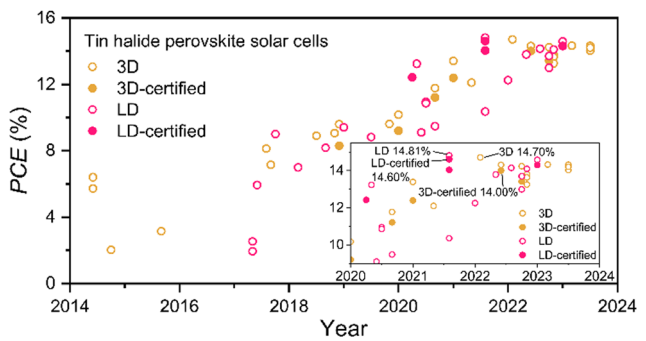

Fig. 4 Evolution of the efficiency of THPSCs based on 3D- and LD-structured THPs.

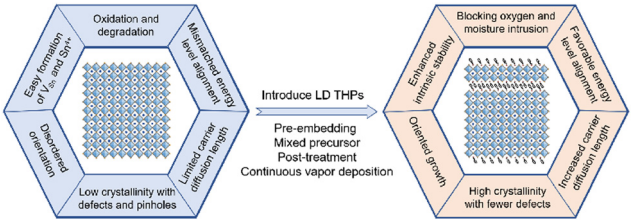

Fig. 6 Breaking the bottleneck of 3D THPSCs by introducing LD structures.

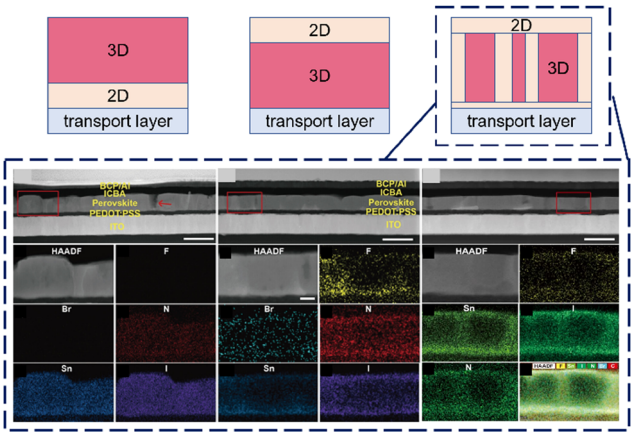

Fig. 7 Different structures of LD/3D THPSCs and STEM images of wrapping structure with corresponding EDX maps.[25] Reproduced from ref. 25 with permission from Wiley-VCH, Copyright 2021.

2.2.2 Optimized dimensionality modulation of LD/3D THPs. Although the efficiency and stability of THPSCs have been improved (Table 1), they are still far from the current state-of-the-art Pb-based PSCs. Here, we analyze and discuss four important aspects of dimensionality for the further improvement of THPSCs, including LD/3D segmentation types, the orientation of LD THPs, the balance of the n value, and optimization of energy level alignment.

In the case of LD/3D structures, three different segmentation types need to be carefully considered (Fig. 7), which have been applied in various works. In these types, the LD phase is located at the bottom or top of the 3D phase, or completely wrapped around the 3D phase, respectively. As previously mentioned, LD THPSCs have demonstrated unique advantages over conventional 3D THPSCs in terms of both efficiency and stability. Therefore, among these structures, we recommend the third one, in which 3D phase perovskite crystallites are completely encapsulated by LD THPs at the upper and lower interfaces and grain boundaries. This segmentation can comprehensively protect the internal 3D phase, passivate surface defects, and improve the film crystalline quality.

Further, the orientation of LD THPs should be modulated to suit the specific application scenario, ensuring efficient carrier transport and improved stability (Fig. 8). When they are located at the bottom or in the bulk, LD THPs with high crystallinity and vertical orientation are preferred, ensuring excellent carrier transport in the device. In contrast, when LD THPs are located on the upper surface as a protective layer, the horizontally grown LD THP layer may provide tight coverage to avoid the exposure of the oxidizable Sn^{2+} sites. We found that various factors such as the electrostatic interactions between different substrates and precursor components, as well as the nucleation barrier of LD THPs, have a significant effect on the oriented growth of the films.[97,98] However, the underlying mechanism for this is still unclear. Based on this mystery, more in-depth and systematic studies are needed for the regulation of the orientation of LD THPs and the underlying mechanism.

In addition to the above-mentioned segmentation type and orientation, the appropriate n value of LD THPs is another important aspect in balancing the efficiency and stability of THPSCs. In the LD/3D system, when employing a low n value such as $n = 1$, the excessively high energy barrier between the LD phase and 3D phase leads to inhibited carrier transport and severe interfacial nonradiative recombination (Fig. 9a). Alternatively, at high n values, THPs are more prone to undergo transitions to oxidized phases with lower formation energy, leading to unfavorable Sn^{4+} and defects, which reduce the overall device stability (Fig. 9b).[72] Hence, suitable n values should be chosen to maintain the balance between carrier transport and stability in THPs (Fig. 9c).

Given that the V_{OC} and PCE losses from nonradiative recombination due to severe energy level mismatch are still issues, the optimization of band alignment should be systematically investigated. Considering that holes and electrons in quasi-2D THPs with different n values flow directionally, the matching between the direction of carrier transport with different quantum well alignments according to their relative

Table 1 Parameters of high-efficiency THPSCs that have been evaluated for operation stability under AM 1.5 G illumination

Structure	V_{OC} (V)	J_{SC} (mA cm^{-2})	FF	PCE (%)	Stability	Ref.
ITO/PEDOT:PSS/$FASnI_3$/C_{60}/BCP/Ag	0.77	22.48	0.70	12.1	Encapsulated, glove box, T_{94} = 500 h	92
ITO/PEDOT:PSS/$FASnI_3$/C_{60}/BCP/Cu	0.80	24.20	0.74	14.2	Encapsulated, in air, T_{95} = 200 h	93
ITO/PEDOT:PSS/$FASnI_3$ + SnF_2 + GeI_2 + $EDABr_2$/C_{60}/BCP/Ag	0.82	22.49	0.77	14.2	Encapsulated, ambient condition, T_{95} = 110 h	94
ITO/PEDOT:PSS/$FASnI_3$ + PHCl-Br/C_{60}/BCP/Ag	0.81	23.02	0.72	13.4	Unencapsulated, glove box, T_{82} = 330 h	63
ITO/PEDOT:PSS/$FASnI_3$ + PAI/C_{60}/BCP/Ag	0.73	22.37	0.72	11.8	Encapsulated, glove box, T_{95} = 1000 h	95
ITO/PEDOT:PSS/$FASnI_3$ + CDTA/C_{60}/BCP/Ag	0.64	21.83	0.74	10.3	Encapsulated, in air with 30% RH, T_{90} = 1000 h	56
ITO/PEDOT:PSS/$FASnI_3$ + TFBAI/C_{60}/BCP/Ag	0.70	21.07	0.74	11.0	Encapsulated, in air, T_{80} = 1643 h	96
ITO/Cu-NiO_x/$FASnI_3$ + $4AMPI_2$/PCBM/Ag	0.69	21.15	0.74	10.9	Unencapsulated, in N_2, 1-sun white LED illumination at 40 °C, T_{77} = 500 h	83

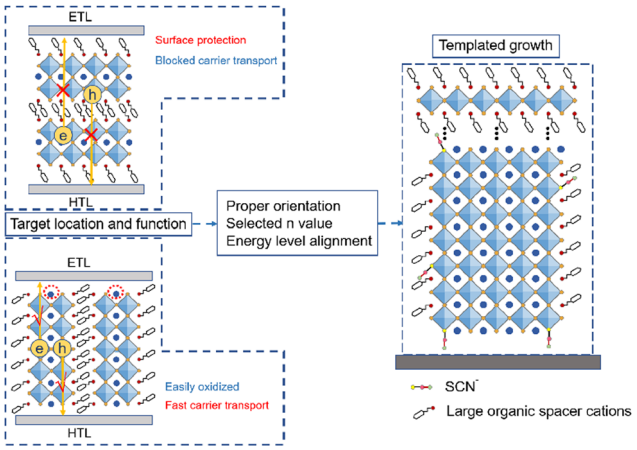

Fig. 8 Orientation optimization of LD THPs.

spatial positions in the LD/3D structure needs to be considered.[96] When the complex phase distributions of the LD/3D THPs cannot be determined, the choice of the device structure should be decided by specifically testing the energy levels of each layer. Moreover, we suggest the introduction of additional methods used in recent advanced studies including those based on 3D THPSCs, such as interfacial treatment,[99,100] dual-site passivation,[94,101] and precursor optimization,[73,102] to synergistically improve the stability and efficiency of LD/3D THPSCs. Also, based on the optimized THPs, the introduction of suitable interfacial modifier molecules and charge transport layers with special structures such as nanorod arrays can further accelerate the carrier extraction, thus breaking the limitation of insufficient carrier diffusion length and achieving higher J_{SC} and PCE by using thicker THP films.

2.3 New 2D perovskites with small ionic radius metal center

While the Pb cations are replaced by other divalent metals besides Sn^{2+} (such as Ge^{2+}, Cu^{2+}, and Zn^{2+}), the newly synthesized perovskites suffer from structural instability.[28] These perovskites experience geometrical constraints and energetically favorable distortion, and finally crystallize into polar non-perovskite structures. Basically, the stability of perovskite structures can be judged by the octahedral factor μ (eqn (2)) and the Goldschmidt tolerance factor[103,104] t (eqn (3)). Values of μ between 0.442 and 0.895 indicate the formation of stable

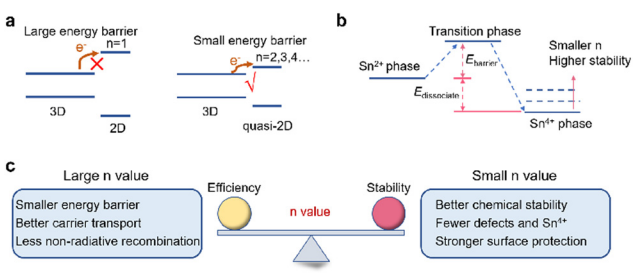

Fig. 9 (a) Energy barriers in LD/3D systems with different n values. (b) Oxidation process of LD THPs with different n values. (c) Balancing factors for n value selection in LD/3D devices.

Table 2 Octahedral factor of the octahedra with Ge, Cu or Zn centers

Octahedra	Octahedral factor μ
$[GeCl_6]^{4-}$	0.403
$[GeBr_6]^{4-}$	0.372
$[GeI_6]^{4-}$	0.332
$[CuCl_6]^{4-}$	0.403
$[CuBr_6]^{4-}$	0.372
$[CuI_6]^{4-}$	0.332
$[ZnCl_6]^{4-}$	0.409
$[ZnBr_6]^{4-}$	0.378
$[ZnI_6]^{4-}$	0.336

octahedra, while a t factor between 1.0 and 0.9 corresponds to the formation of a cubic structure. When the t factor decreases to 0.8–0.89, the corresponding perovskite undergoes distortion, resulting in the formation of an orthorhombic,[105] rhombohedral, or tetragonal structure. Moreover, a t factor below 0.8 leads to the formation of an alternative structure such as ilmenite, while a t factor exceeding 1 results in a hexagonal structure.[106] Thus, an inappropriate composition may induce lattice distortion and even the degradation of the crystallinity, which result in an increase in the defect density and severe electron–phonon coupling.

$$\mu = \frac{R_B}{R_X} \quad (2)$$

$$t = \frac{(R_A + R_X)}{\sqrt{2}(R_B + R_X)} \quad (3)$$

Previous research reported that Ge substitution prefers a structure of trigonal pyramidal $[GeI_3]^-$ units, while its Cu and Zn counterparts prefer square planar and tetrahedron, respectively.[107,108] The variation in structure originates from the relatively small ionic radius metal center, which leads to a small octahedral factor μ (Table 2), resulting in the destruction of the octahedra. Recently,[28] Sargent *et al.* reported a new design of low-dimensional Ge-based perovskite (Fig. 10), allowing for stable low-dimensional perovskites with small ionic radius metal center. Compared to the non-perovskite structure, the $[GeI_6]^{4-}$ octahedra exhibit a direct bandgap with a significant redshift. Additionally, they have 10-times less octahedral distortion according to the single-crystal X-ray diffraction data, and 10-times higher electron and hole mobility based on DFT calculations. These improved aspects of new materials approach the requirements of photovoltaic applications. This new concept of

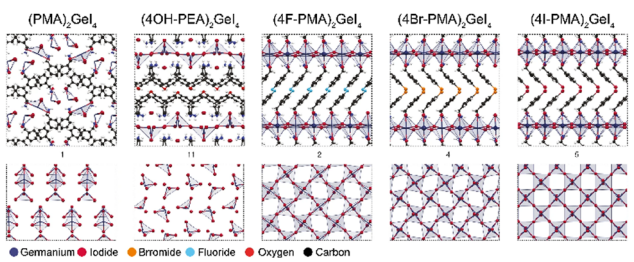

Fig. 10 New design of low-dimensional Ge-based perovskite.[28] Reproduced from ref. 28 with permission from Springer Nature, Copyright 2023.

using intermolecular bonds to scaffold 2D perovskite will further advance lead-free perovskite-based optoelectronics.

3. Elevating electronic dimensionality in double perovskites

Double perovskites, which are typically composed of monovalent and trivalent metal-centered octahedra (*e.g.*, $Cs_2AgBiBr_6$), are another category of lead-free perovskites (Fig. 11). To date, numerous double perovskites have been achieved experimentally, with monovalent metals[109] such as Li^+, Na^+, K^+, Rb^+, Cu^+, Ag^+, In^+, and Tl^+ and trivalent metals such as In^{3+}, Tl^{3+}, Bi^{3+}, Sb^{3+} and other transition metals (Fig. 12). However, not all of these possible candidates are structurally stable due to the existence of geometrical constraints and energetically favorable distortion. Finally, inappropriate central metals lead to the severe distortion of the octahedra, which may trap the photogenerated charge carriers.[29]

According to the parameters influencing the PCE (eqn (1)), it is better to choose a composition with high absorbance and narrow bandgap. Hence, we should first consider the transition type, including inversion symmetry and phonon participation. Meng *et al.*[110] analyzed the optical absorption properties of double perovskite and found six types of direct bandgaps (Fig. 13a). Only one type of compounds with In^+/Tl^+ monovalent cations and Sb^{3+}/Bi^{3+} trivalent cations is appropriate with strong transition. However, the intrinsic chemical instability of In^+ and the high toxicity of the Tl metal directly exclude them. Hence, the promising candidates are only the type with an intrinsic indirect bandgap, which combines Cu^+, Ag^+ or Au^+ monovalent cation and Sb^{3+} or Bi^{3+} trivalent cation. Among these compounds, $Cs_2AgBiBr_6$ is the most evaluated and investigated, which possesses an intrinsic indirect bandgap of 1.95 eV.[31]

Three main aspects limit the application of $Cs_2AgBiBr_6$ in PSCs, including its relatively large bandgap as the absorber in single-junction PSCs; indirect bandgap; and intrinsic short charge carrier diffusion length due to the 0D electronic dimensionality and strong electron–phonon coupling.[17,109] Although the intrinsic large bandgap of $Cs_2AgBiBr_6$ can be narrowed by iodide doping or substitution, successful correlated devices still have not yet been achieved. Due to the relatively unstable structure of Cs_2AgBiI_6, a polymorph containing $Cs_3Bi_2I_9$ is always synthesized during fabrication.[111] Besides, A-site doping or substitution of 3D-$Cs_2AgBiBr_6$ has no significant contribution to the band structure according to the DFT calculation,[112] and thus fails to adjust the bandgap. Specifically, the CBM and VBM of $Cs_2AgBiBr_6$ are predominantly composed of Bi-p and Ag-d states, respectively (Fig. 13b).

To date, an effective way to narrow the bandgap of $Cs_2AgBiBr_6$ is through B-site doping or substitution.[113–115] By partially replacing Ag^+ with Cu^+/Cu^{2+}, the absorption edge can be extended from 610 nm to 860 nm.[113] In addition, the addition

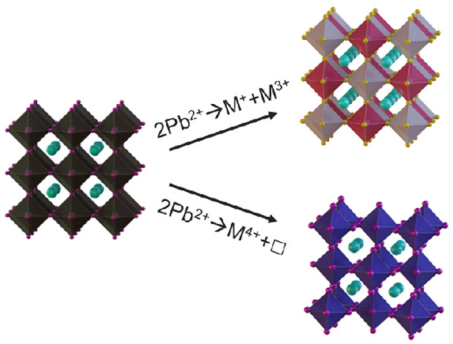

Fig. 11 Schematic of the double perovskite structure.

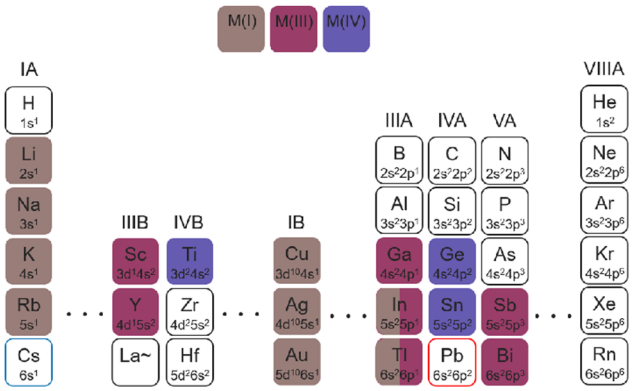

Fig. 12 B-site elements for the fabrication of double perovskites in the periodic table.

a

B3+ \ B+		Group 3	Group 13	Group 15
		Sc, Y	Al, Ga, In(3+), Tl(3+)	Sb(3+), Bi (3+)
Group 1	Na, K, Rb, Cs	Direct (*All forbidden*)	Direct (*All forbidden*)	Mostly Direct (*Weak transition*)
Group 11	Cu, Ag, Au	Indirect	Direct (*partial forbidden*)	Indirect
Group 13	In(1+), Tl(1+)	Direct (*Weak transition*)	Indirect	Direct (*Strong transition*)

b

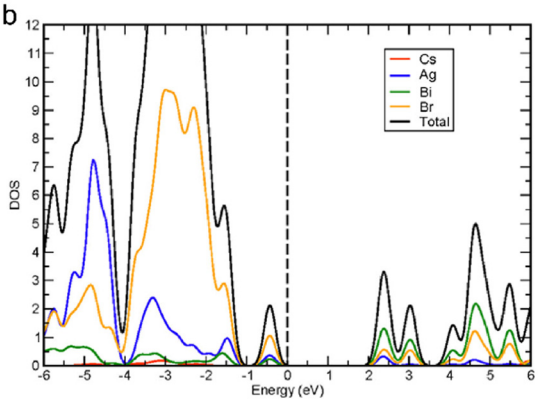

Fig. 13 (a) Possible combinations for $A_2B^+B^{3+}X_6$ double perovskite.[110] Reproduced from ref. 110 with permission from the American Chemical Society, Copyright 2017. (b) Atomic partial density of states plots for $Cs_2AgBiBr_6$.[112] Reproduced from ref. 112 with permission from the American Chemical Society, Copyright 2016.

of $FeBr_2$ results in an extension of the light absorption edge from 610 nm to 1350 nm with 1% Fe doping.[114] Nevertheless, these methods lack the consideration of reversing the situation of indirect bandgap and short charge carrier diffusion length. Numerous computation efforts have been devoted to exploring how to turn the direct bandgap of $Cs_2AgBiBr_6$ to an indirect one by elemental doping or substitution. For example, influenced by the B-site alloying of In, the calculation results demonstrated a reduced direct bandgap of 1.85 eV in $Cs_2AgBi_{0.25}In_{0.75}Br_6$.[116] However, few experimental counterparts have been reported according to these computational discoveries.

One effective way to reverse the indirect bandgap of $Cs_2AgBiBr_6$ is reducing its dimensionality down to a 2D layered form. Inspired by the divalent 2D perovskite, double perovskite can also be synthesized into a monolayer structure with a Ruddlesden–Popper-phase of $(RA)_4AgBiBr_8$, where RA represents different primary ammonium large cations with alkyl- and/or aryl-based functionalities.[117] The calculated results revealed that when the thickness is reduced to a monolayer, $Cs_2AgBiBr_6$ moves from an indirect bandgap to a direct bandgap material (Fig. 14a).[118,119] However, despite its enhanced effective hole mass, the hole mobility of monolayer $Cs_2AgBiBr_6$ is increased due to the specificity of its 2D structure with a direct bandgap (Fig. 14b and c). Moreover, the 2D structure can stabilize the unstable iodide counterparts, which have prospectively lower bandgaps,[120] making them promising for photovoltaic application. The reduced dimensionality can also be achieved in the Dion-Jacobson-phase (Fig. 15), utilizing Ru or Mo as the trivalent metal,[121] in which the bandgaps are tunable according to the layer composition, but are largely independent of the spacer. The dimensionality-reduced derivatives of double perovskites can significantly enhance the flexibility of halide perovskites for substitutions and allow for greater diversity in composition and electronic properties.

In the case of the intrinsic short charge carrier diffusion length due to the 0D electronic structure and strong self-trapping effects, the crucial point is to avoid the formation of the special ordering structure of isolated band-edge-deriving octahedra.[30] Unlike the normal electronic-3D perovskites such as $CsPbBr_3$ with a direct bandgap and excellent charge transport property, $Cs_2AgBiBr_6$ with this special ordering structure exhibits a wide indirect bandgap and large carrier effective mass.[122] Specifically, the isolated band-edge-deriving octahedra of Ag and Bi result in discontinuous frontier electronic orbitals, leading to an electronic-0D structure (Fig. 16). Also, the isolated excited state may easily cooperate with the lattices and cause severe self-trapping of charges. According to DFT calculation, the indirect bandgap of $Cs_2AgBiBr_6$ can be tuned to a direct bandgap by changing it from an ordered system to disordered one following the disordering of Ag^+/Bi^{3+} cations by creating anti-site defects in its sublattice (Fig. 17).[123] Simultaneously, the bandgap decreases from 2.04 eV to 1.59 eV, which approaches the appropriate bandgap for single-junction PSCs. Experimentally, inspired by this concept, Klarbring *et al.* achieved a bandgap of 1.72 eV for $Cs_2AgBiBr_6$ under ambient

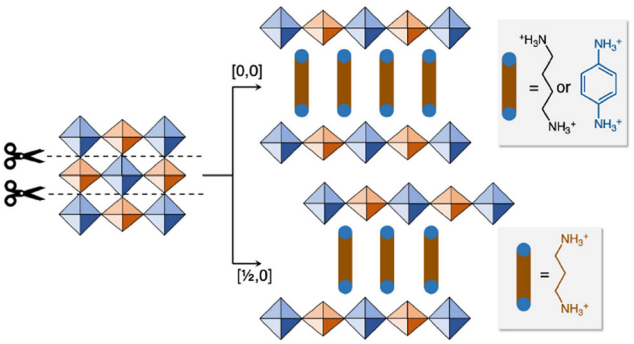

Fig. 15 Two-dimensional double perovskite in Dion–Jacobson phase.[121] Reproduced from ref. 121 with permission from the American Chemical Society, Copyright 2022.

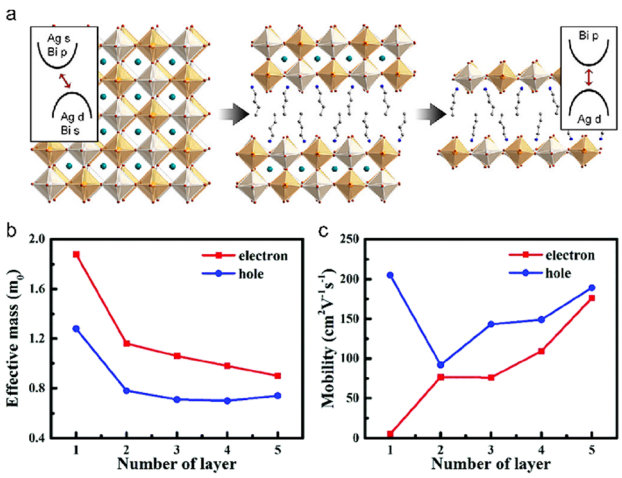

Fig. 14 (a) Schematic of the dimensionality correlated bandgap.[118] Reproduced from ref. 118 with permission from the American Chemical Society, Copyright 2018. Calculated effective mass (b) and mobility (c) of electrons and holes in $Cs_2AgBiBr_6$.[119] Reproduced from ref. 119, CC BY.

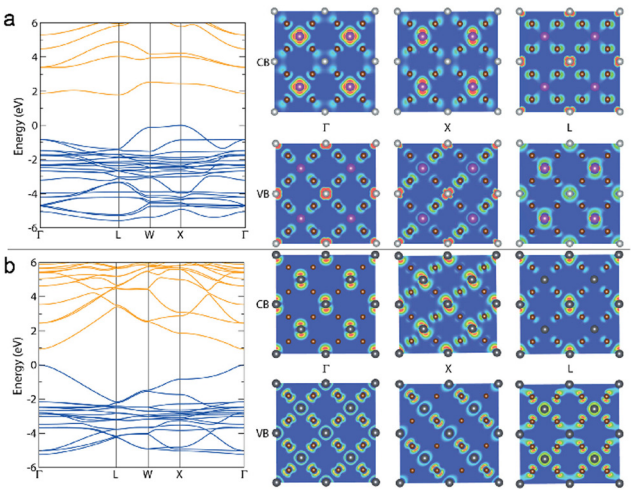

Fig. 16 Band structures of (a) $Cs_2AgBiBr_6$ and (b) $CsPbBr_3$, with respective charge density isosurfaces of the VBM and CBM. Silver atoms are in light gray, bismuth is in purple, lead is in dark gray, and bromine is in brown.[122] Reproduced from ref. 122, CC BY.

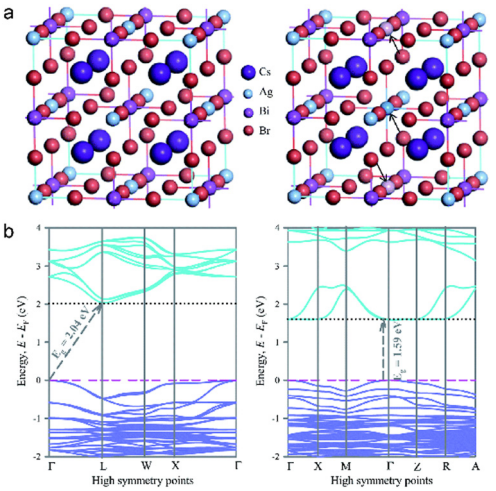

Fig. 17 Crystal structure (a) and band structure (b) of ordered (left) and disordered (right) phase of $Cs_2AgBiBr_6$.[123] Reproduced from ref. 123, CC BY.

conditions through a novel crystal-engineering strategy.[124] Another effective way to reverse the special ordering structure of $Cs_2AgBiBr_6$ is through B-site doping or substitution, which can significantly modulate its band structure. However, the successful cases such as Tl or In(I) doping or substitution with rebuilt band structures suffer from toxicity and instability problems, respectively.[122,124] We conclude that this improvement is a 0.5-dimensionality increase in the electronic structure, which partially breaks the isolated band-edge-deriving octahedra and reconnect the isolated frontier electronic orbitals. Moreover, Ji *et al.* successfully synthesized three compounds with a B-site columnar-ordered structure (Fig. 18),[125] which exhibited small bandgaps in the range of 1.33–1.77 eV and small carrier effective masses along the octahedra chains. Due to the columnar ordering (electronic-1D), the electronic properties of these compounds were anisotropic, wherein the effective masses for holes and electrons along the direction parallel to the octahedral chains were relatively small. In addition, the self-trapping effects can potentially be tuned by elevating the electronic dimensionality. However, enhanced devices based on these dimensionality elevating methods are still lacking due to the technical bottleneck of special film fabrication.

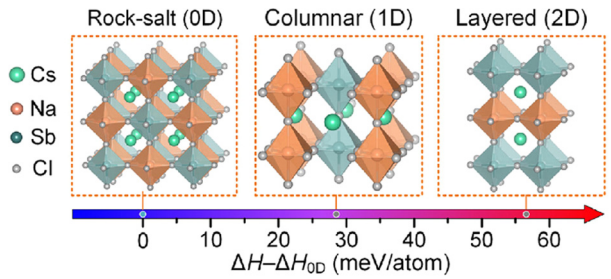

Fig. 18 Formation enthalpies of $Cs_2NaSbCl_6$ double perovskite with columnar-ordered (1D) and layered-ordered (2D) arrangements, with respect to that with the rock-salt-ordered (0D) arrangement.[125] Reproduced from ref. 125 with permission from American Chemical Society, copyright 2021.

Inspired by the modification of inorganic semiconductors *via* ion implantation,[126] double perovskites can also be modified by this technique. Thereby, the interstitial doping of double perovskites can be achieved, and the electronic properties of double perovskites can be significantly changed. Experimentally, Zhang *et al.*[127] succeeded in the interstitial doping of atomic hydrogen in the $Cs_2AgBiBr_6$ lattice, which was evidenced by TEM and XRD characterization, resulting in adjusted band energy levels, enhanced carrier mobility and increased carrier lifetime (Fig. 19). Finally, they realize the highest PCE of 6.37% in a $Cs_2AgBiBr_6$-based PSC. We conclude that this improvement is due to the 3-dimensionality increase in the electronic structure, which not only adjusts the valence and conduction band energy levels, but also optimizes the carrier mobility and carrier lifetime. Another type of double perovskite with vacancy-ordered structure (*e.g.*, Cs_2SnI_6) can also benefit from this interstitial doping method. In this structure, the octahedra of tetravalent metals and halides are isolated in coordination similar to a perovskite structure but with octahedral voids in each adjacent position.[128] Although these octahedra are not connected, the space between them can be narrowed independently of the size of the octahedra. Zhang *et al.* found that after interstitial doping of Li^+, intermediate energy levels were created and the absorption edge redshifted.[129] The experimental results showed no lattice change but significantly enhanced carrier mobility (356.6 $cm^2\ V^{-1}\ s^{-1}$), which was elucidated by the variation in the electronic distribution, and thus elevated electronic dimensionality.

Although the PCE of double-perovskite-based PSCs remains inferior, the potential enhancement in their stability compared to lead-based perovskites, especially in high moisture and high temperature environments, makes this category of lead-free

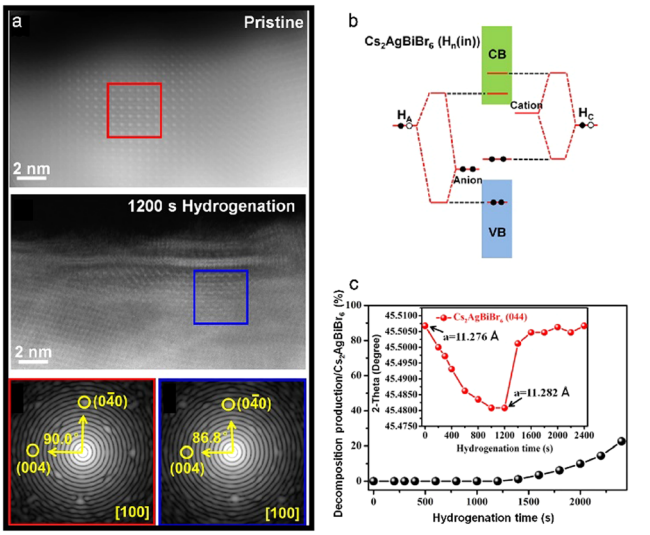

Fig. 19 (a) HAADF and Fast Fourier transform (FFT) images of pristine and hydrogenated $Cs_2AgBiBr_6$ films. (b) Schematic band coupling models in hydrogenated $Cs_2AgBiBr_6$ films. (c) Evolution tendency for the XRD area proportion of CsBr (110) peak during the hydrogenation treatment.[127] Reproduced from ref. 127, CC BY.

perovskites hopeful and competitive alternatives. Thus, the concept of electronic dimensionality in this category of lead-free perovskites may be leveraged to further breakthrough the PCE bottleneck.

4. Manipulating the dimensionality in defect-structured perovskites

4.1. $A_3B_2X_9$ perovskites

$A_3B_2X_9$ is another category of lead-free perovskites for photovoltaic applications (Table 3), which is formed by the complete substitution of the B-site with a trivalent cation such as Sb^{3+} and Bi^{3+}. Given that they are adjacent to Pb in the periodic table, thus maintaining a similar electronic configuration, Bi and Sb are considered competitive candidates for the substitution of Pb in the perovskite absorber due to their potential strong light absorption and long carrier lifetime. On account of the different connection types of $[BX_6]^{3-}$ octahedra, $A_3B_2X_9$ exhibits different polymorphs, including the 0D-dimer conformation consisting of isolated $[B_2X_9]^{3-}$ units[35,130] and 2D-layer conformation with double octahedral layers and B-site vacancies between them (Fig. 20).[35,131] Generally, the 2D-layer conformation is thermodynamically preferred when using either small A-site cations such as K^+,[132] Rb^+,[133] and NH_4^+[134] or small X-site anions such as Br^-[135] and Cl^-,[136] while the 0D-dimer conformation will be dominant when large A-site cations such as FA^+, MA^+, and Cs^+ are introduced.

4.1.1. 0D-dimer conformation. $A_3B_2X_9$ in the 0D-dimer conformation (Fig. 21a) is usually accompanied by a large indirect bandgap, large carrier effective mass and the easy formation of deep defects. Consequently, its performance is rather disappointing.[12] For example, theoretical calculations revealed that $Cs_3Bi_2I_9$ exhibits a large indirect bandgap of 2.10 eV (Fig. 21b), resulting in a low absorption coefficient as well as the inadequate utilization of the whole solar spectrum.[175] The VBM of the 0D-dimer conformation is derived from the I 5p orbitals slightly hybridized with Bi 6s orbitals, while the CBM is composed of Bi 6p and I 5p orbitals (Fig. 21c).[176] Therefore, the isolation of $[Bi_2I_9]^{3-}$ dimers leads to the localization of the VBM and the CBM, which is the primary reason for the large carrier effective masses, and consequently poor carrier mobility.[177,178] In addition, most of the defects in $Cs_3Bi_2I_9$ possess a low formation energy and tendency to generate deep level states in the bandgap, leading to strong recombination.[138,177] Similar issues were observed in $Cs_3Sb_2I_9$, indicating that these drawbacks are common in 0D-dimer-structured $A_3B_2X_9$ perovskites and pose significant challenges for achieving high-efficiency photovoltaic devices based on this conformation.

Basically, the challenges associated with the 0D-dimer-structured $A_3B_2X_9$ mainly originate from its low-dimensional structure. Moreover, affected by the strong distortion of the $[BiX_6]^{3-}$ and $[SbX_6]^{3-}$ octahedra, which induces a strong self-trapping effect, the free motion of charge carriers is further prohibited, resulting in an even smaller mobility.[179] Thus, to alleviate this structural-induced predicament in 0D-dimer-structured $A_3B_2X_9$, dimensionality modulation is proposed as an effective solution to enhance the optoelectronic properties of $A_3B_2X_9$ through conformation modifications, which can be achieved by optimizing the composition of the precursor and introducing a large-size organic cation.

The addition of excess BiI_3 to the precursor solution has the potential to passivate the Bi^{3+} vacancies, which is beneficial for carrier transport.[138] Moreover, due to the 2D nature of the conformation (Fig. 22a), BiI_3 would facilitate the rearrangement of adjacent octahedra from a face-sharing $[Bi_2I_9]^{3-}$ dimer to a corner-sharing $[BiI_6]^{3-}$ along the *a* and *b* directions, thereby allowing the system to attain elevated dimensionality, and thus increased mobility.[138,139] Besides, it is worth noting that adjusting the appropriate ratio of CsI and BiI_3 in the precursor can lead to the formation of $CsBi_3I_{10}$, which exhibits a smaller direct bandgap and better carrier mobility (Fig. 22b). By connecting the isolated $[Bi_2I_9]^{3-}$ through a corner-sharing way, $CsBi_3I_{10}$ breaks the original isolation and improves the electronic dimensionality (Fig. 22c), resulting in a significantly improved PSC performance.[180,181]

The introduction of large organic cations may rebuild the electronic structure of 0D-dimer perovskites owing to the spatially connected carrier transport path (Fig. 23a). Therefore, this hybrid structure exhibits enhanced carrier transport and elevated electronic dimensionality. In addition, the distance between dimers is enlarged due to the steric effect of large organic cations, leading to a decrease in bandgap (Fig. 23b).[182,183] Also, this variation in structure changes the original indirect bandgap to a direct bandgap.

4.1.2. 2D-layer conformation. Another pathway to elevate the dimensionality of $A_3B_2X_9$ is directly turning the 0D-dimer conformation into a 2D-layer one (Fig. 24a), which can be achieved by employing a small A-site, B-site and X-site composition (Fig. 20). Generally, the 2D-layer conformation enjoys better carrier mobility, and thus improved performance because of its higher structural dimensionality and the corresponding electronic dimensionality. For instance, the 2D-layer $Cs_3Sb_2I_9$ has a near direct bandgap of 2.04eV at the Γ point, leading to a significantly enhanced absorption compared with that of the 0D-dimer conformation (Fig. 24b).[184] The VBM of 2D-layer $Cs_3Sb_2I_9$ is primarily composed of I 5p orbitals with a slight hybridization with the Sb 5s orbitals, while its CBM consists of I 5p and Sb 5p orbitals (Fig. 24c). Therefore, the formation of 2D layer breaks the isolation of octahedra in the 0D-dimer conformation, resulting in the better connection of the electronic orbitals, and hence higher mobility. Consequently, the defect issue is well addressed after turning $A_3B_2X_9$ from the 0D-dimer conformation to the 2D-layer one.[36] Furthermore, the enhancement in phase purity of the 2D-layer conformation is also beneficial for reducing the density of defects.[171]

However, despite the improvement compared with its 0D counterpart, 2D-layer $A_3B_2X_9$ still suffers from the limitation of carrier transport in the vertical direction of the 2D-layer plane. In the case of PSCs, which consist of an absorption layer sandwiched between transport layers, effective carrier transport

Table 3 Summary of reported Bi-based and Sb-based $A_3B_2X_9$ PSCs

Compound	Structure	Method	Dimension	Bandgap (eV)	PCE (%)	Ref.
$Cs_3Bi_2I_9$	FTO/c-TiO_2/m-TiO_2/$Cs_3Bi_2I_9$/spiro-OMeTAD/Ag	Normal spin-coating	0D	2.20	1.09	136
	FTO/c-TiO_2/m-TiO_2/$Cs_3Bi_2I_9$/spiro-OMeTAD/Au	Anti-solvent	0D	2.20	0.18	137
	FTO/c-TiO_2/$Cs_3Bi_2I_9$/CuI/Au	Dissolution–recrystallization method	0D	2.30	3.20	20
	FTO/m-TiO_2/$Cs_3Bi_2I_9$/spiro-OMeTAD/Au	20% excess BiI_3	0D	1.70^{in}	0.21	138
	FTO/c-TiO_2/m-TiO_2/$Cs_3Bi_2I_9$/TQ1/Au	CsI : BiI_3 = 1 : 1	0D	1.77	0.62	139
	AZO/c-TiO_2/$Cs_3Bi_2I_9$/CuSCN/Graphite	Normal spin-coating	0D	2.19^{in}	0.17	140
	FTO/c-TiO_2/m-TiO_2/$Cs_3Bi_2I_9$/CuI/Au	Polar solvent treatment	0D	2.00	1.09	141
	FTO/c-TiO_2/m-TiO_2/$Cs_3Bi_2I_9$/spiro-OMeTAD/Au	Solvent vapor annealing	0D	1.70	0.98	142
	FTO/c-TiO_2/m-TiO_2/$Cs_3Bi_2I_9$/spiro-OMeTAD/Au	Polar solvent treatment	0D	2.10	1.66	143
	FTO/c-TiO_2/m-TiO_2/$Cs_3Bi_2I_9$/C	KI doping	0D	1.83	2.81	144
	ITO/NiO_x/$Cs_3Bi_2I_9$/$PC_{61}BM$/C_{60}/BCP/Ag	Chlorobenzene treatment	0D	1.85^{in}, 2.23^{d}	0.23	135
	ITO/NiO_x/$Cs_3Bi_2I_{9-x}Br_x$/$PC_{61}BM$/C_{60}/BCP/Ag	Br^- doping & Chlorobenzene treatment	2D	1.75^{in}, 2.05^{d}	1.15	135
	FTO/TiO_2/$Cs_3Bi_2I_9$/CuI/Au.	Vapor transport deposition	0D	$1.72–2.20^{in}$	1.52	145
	FTO/c-TiO_2/m-TiO_2/$Cs_3Bi_2I_9$/CuSCN/Au	Rb^+ doping	0D	2.04^{d}	1.17	146
	ITO/NiO_x/$Cs_3Bi_2I_9$/$PC_{61}BM$/BCP/Ag	Ligand-assisted reprecipitation	0D	2.05	0.70	147
$MA_3Bi_2I_9$	FTO/c-TiO_2/m-TiO_2/$MA_3Bi_2I_9$/spiro-OMeTAD/Ag	Normal spin-coating	0D	2.10	0.12	136
	FTO/c-TiO_2/m-TiO_2/$MA_3Bi_2I_9$/spiro-OMeTAD/MoO_3/Ag	Normal spin-coating	0D	2.10	0.42	148
	ITO/PEDOT:PSS/$MA_3Bi_2I_9$/C_{60}/BCP/Ag	Two-step spin-coating	0D	2.22	0.39	149
	FTO/c-TiO_2/m-TiO_2 + MAIB/MAIB/spiro-OMeTAD/Au	Anti-solvent	0D	2.10^{d}	0.356	150
	FTO/m-TiO_2/$MA_3Bi_2I_9$/spiro-OMeTAD/Ag	Gas-assisted coating	0D	2.06	0.082	151
	FTO/m-TiO_2/$MA_3Bi_2I_9$/spiro-OMeTAD/Ag	Sequential vacuum vapor deposition	0D	2.26	1.64	152
	FTO/c-TiO_2/m-TiO_2/$MA_3Bi_2I_9$/spiro-OMeTAD/Au	S^{2-} doping	0D	1.67	0.152	153
	FTO/c-TiO_2/m-TiO_2/$MA_3Bi_2I_9$/P3HT/Au	Anti-solvent	0D	2.39^{in}	1.09	154
	FTO/c-TiO_2/m-TiO_2/$MA_3Bi_2I_9$/P3HT/Ag	Sn^{4+} doping	0D	1.91	0.91	155
	FTO/c-TiO_2/$MA_3Bi_2I_9$/spiro-OMeTAD/Au	Two-step spin-coating	0D	1.82	1.53	156
	FTO/c-TiO_2/$MA_3Bi_2I_9$/spiro-OMeTAD/Au	Two-step spin-coating	0D	2.05	1.31	157
$Cs_3Sb_2I_9$	ITO/PEDOT:PSS/$Cs_3Sb_2I_9$/$PC_{70}BM$/C_{60}/BCP/Al	HI additive	0D	2.00	0.84	158
	FTO/c-TiO_2/m-TiO_2/$Cs_3Sb_2I_9$/spiro-OMeTAD/Au	Anti-solvent	0D	2.43^{in}	0.76	159
	ITO/PEDOT:PSS/D-$Cs_3Sb_2I_9$/$PC_{71}BM$/Al	NMP additive & vapor annealing	0D	2.13^{d}, 2.37^{in}	1.86	160
	ITO/PEDOT:PSS/$Cs_3Sb_2I_9$/PCBM/Al	ITIC treatment & vapor annealing	0D	2.05^{d}	3.25	161
	FTO/c-TiO_2/m-TiO_2/$Cs_3Sb_2I_9$/spiro-OMeTAD/Au	Thiourea additive & vapor annealing	0D	2.05	2.22	162
	FTO/c-TiO_2/$Cs_3Sb_2I_9$/P3HT/C	Anti-solvent	0D	2.00	2.50	163
	ITO/PEDOT:PSS/$Cs_3Sb_2I_9$/$PC_{70}BM$/C_{60}/BCP/Al	Normal spin-coating & vapor annealing	2D	2.05^{d}	1.49	164
	FTO/c-TiO_2/$Cs_3Sb_2I_9$/Au	HCl additive & anti-solvent	2D	2.05^{d}	1.21	36
	FTO/c-TiO_2/Sb-PIM/P3HT/Au	MA^+, FA^+, Cl^- doping & anti-solvent	2D	2.10^{d}	2.47	165
	FTO/c-TiO_2/$Cs_3Sb_2I_9$/spiro-OMeTAD/Au	MACl additive & low-pressure assisted	2D	2.05^{d}	3.20	166
$Cs_3Sb_2Cl_xI_{9-x}$	FTO/Nb_2O_5/$Rb_{0.15}Cs_{2.85}Sb_2I_{9-x}Cl_x$/P3HT/C	Rb^+ doping & anti-solvent & vapor annealing	2D	2.07^{d}	2.46	167
	FTO/Nb_2O_5/$Cs_3Sb_2I_{9-x}Cl_x$/P3HT/C	Anti-solvent & vapor annealing	2D	2.07^{d}	1.67	168
	ITO/PEDOT:PSS/$Cs_3Sb_2I_{9-x}Cl_x$/PCBM/Al	Vapor annealing	2D	2.00^{d}	3.42	22
	FTO/Nb_2O_5/$Cs_3Sb_2I_{9-x}Cl_x$/P3HT/C	RbCl pre-treatment & vapor annealing	2D	2.07^{d}	3.37	169
$(NH_4)_3Sb_2I_9$	ITO/PEDOT:PSS/$(NH_4)_3Sb_2I_9$/$PC_{61}BM$/Al	Br^- doping	2D	2.27^{d}	0.51	170
$MA_3Sb_2Cl_xI_{9-x}$	ITO/c-TiO_2/m-TiO_2/$MA_3Sb_2Cl_xI_{9-x}$/spiro-OMeTAD/Au	SbI_3 : MAI : MACl = 1 : 1 : 1.2 & anti-solvent	2D	2.01^{d}	2.19	171
$MA_3Sb_2I_9$	ITO/Cu:NiO/$MA_3Sb_2I_9$/ZnO/Al	Sn^{4+} doping & anti-solvent	0D	1.55	2.69	172
$Rb_3Sb_2I_9$	ITO/c-TiO_2/m-TiO_2/$Rb_3Sb_2I_9$/spiro-OMeTAD/Au	Br^- doping & anti-solvent	2D	2.02^{in}	1.37	133
$MA_3Sb_2I_{9-x}Cl_x$	FTO/c-TiO_2/m-TiO_2/$MA_3Sb_2I_{9-x}Cl_x$/spiro-OMeTAD/Au	Li-TFSI additive & anti-solvent	2D	$1.95–2.23^{d}$	3.34	173
$MA_3Sb_2I_9$	ITO/m-TiO_2/$MA_3Sb_2I_9$/spiro-OMeTAD/Au	Normal spin-coating	2D	2.10^{d}	0.54	174

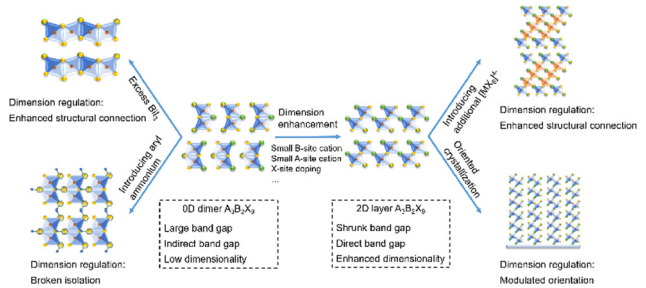

Fig. 20 Dimensionality modulation for defect-structured $A_3B_2X_9$ perovskites.

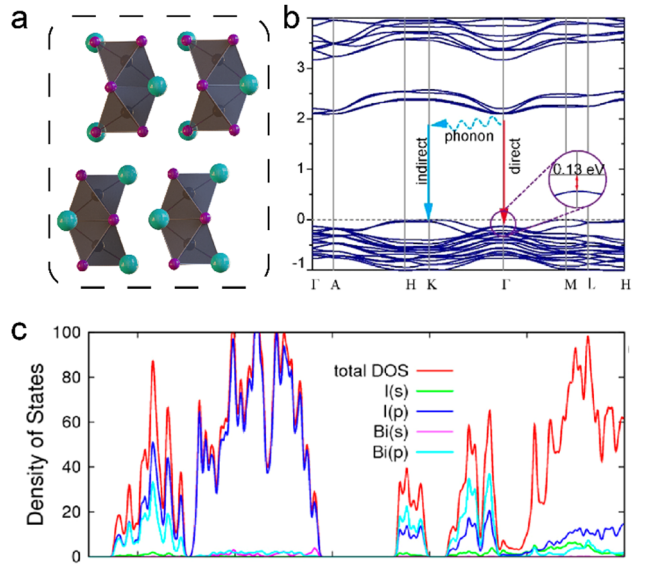

Fig. 21 Crystal structure (a), band structure (b) and partial density of states (c) of the 0D-dimer conformation.[175,176] Reproduced from ref. 175 and 176 with permission from the American Chemical Society, Copyright 2017.

in the vertical direction is vital for the device performance. Specifically, the statistical electronic dimensionality perpendicular to the substrate is crucial. Therefore, the further focus of dimensionality modulation in 2D-layer $A_3B_2X_9$ should be the modulation of its electronic dimensionality perpendicular to the substrate. The orientation of octahedra can be modulated by crystallization optimization, leading to enhanced carrier transport in PSCs. By introducing thiourea in $Cs_3Sb_2I_{9-x}Cl_x$, the C=S functional group could regulate the crystallization dynamics through coordination with Sb^{3+} and generate the (201) preferred orientation.[162] Besides, MACl could also serve as an additive to regulate the crystallization of $Cs_3Sb_2I_{9-x}Cl_x$ by providing excess Cl for the substitution of iodine and generating an intermediate phase for modulated crystallization. The resultant $Cs_3Sb_2I_{9-x}Cl_x$ in the (201) direction with a higher crystallinity successfully improves the carrier transport in devices.[166] Compared with the orientation of the octahedra, the orientation of the 2D-layer plane is more worthy of our attention. We prefer a vertical orientation of 2D-layer $A_3B_2X_9$ than a horizontal orientation (Fig. 25).

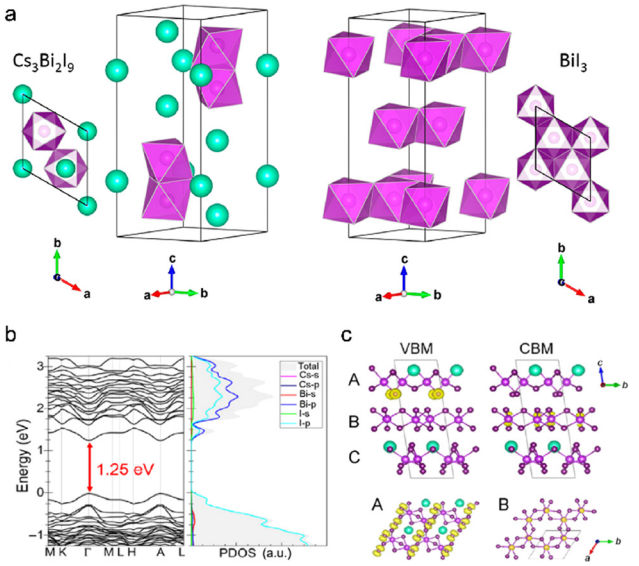

Fig. 22 (a) Crystal structures of $Cs_3Bi_2I_9$ and BiI_3. Green balls represent Cs and purple balls Bi, and I atoms are minimized to simplify the structural view. (b) Band structure and partial density of states of $CsBi_3I_{10}$.[139] Reproduced from ref. 139 with permission from the American Chemical Society, Copyright 2019. (c) Electron distributions at the VBM and CBM of $CsBi_3I_{10}$.[181] Reproduced from ref. 181 with permission from Springer Nature, Copyright 2018.

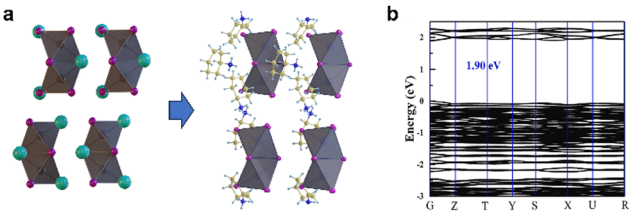

Fig. 23 Dimensionality modulation for defect-structured $A_3B_2X_9$ perovskites.[182] Reproduced from ref. 182 with permission from Elsevier Publishing, Copyright 2023.

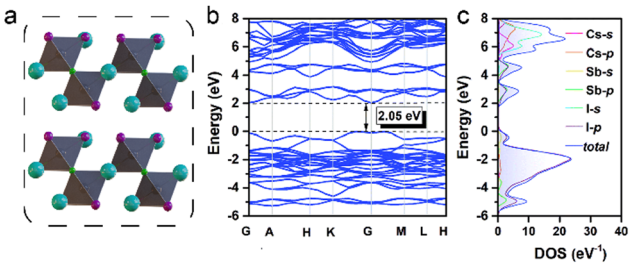

Fig. 24 Crystal structure (a), band structure (b) and partial density of states (c) of 2D-layer conformation.[184] Reproduced from ref. 184 with permission from RSC Publishing, Copyright 2020.

The elevation of electronical dimensionality can also be achieved by introducing additional atoms that can contribute to the 3D structure. Theoretical analysis revealed that the

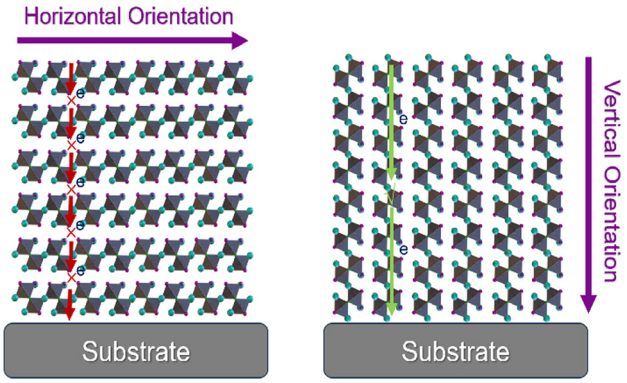

Fig. 25 Schematic illustration of the horizontal and vertical orientations of 2D-layer $A_3B_2X_9$ relative to the substrate.

introduction of a divalent cation including Cu^{2+}, Sn^{2+} and Ge^{2+} in $Cs_3Sb_2X_9$ can result in the formation of $Cs_{3+n}M(II)_nSb_2X_{9+3n}$ (M = Sn, Ge) by inserting $[MX_6]$ between the original octahedral layers, boosting the layer connection, and thus improving the electronic dimensionality in the process (Fig. 26a).[185] Furthermore, given that these M-site atoms can have strong p–p transition with the X-site atoms, the bandgap would be significantly red-shifted, overcoming the large bandgap issue that hinders the performance of PSCs. Furthermore, the enhanced connection of octahedral layers leads to a reduced carrier effective mass (Fig. 26b), resulting in improved carrier transport.

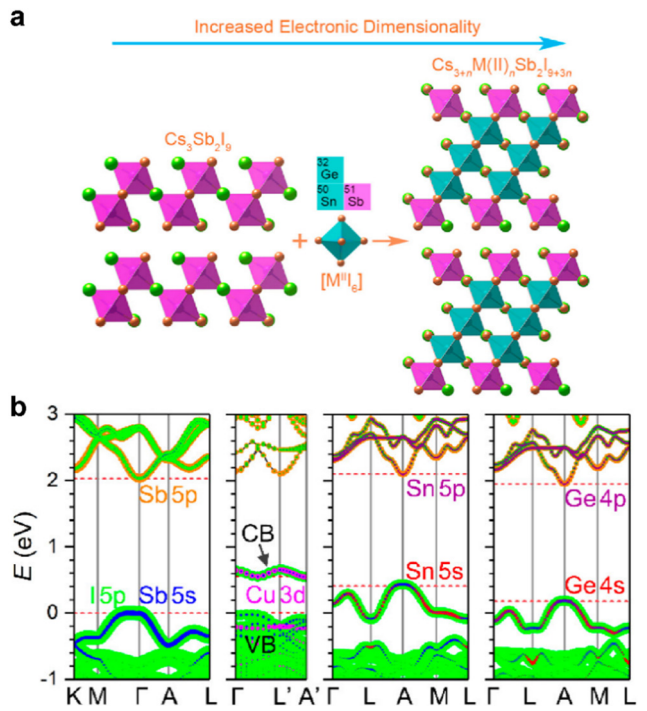

Fig. 26 (a) Schematic illustration of the general design principle for the layered halide double perovskites $Cs_{3+n}M(II)_nSb_2X_{9+3n}$ (M = Sn, Ge). (b) Variation in band structure before and after the introduction of Cu^{2+}, Sn^{2+} and Ge^{2+}.[185] Reproduced from ref. 185 with permission from the American Chemical Society, Copyright 2018.

Despite the fact that dimensional regulation optimizes the performance of 0D dimer $A_3B_2X_9$ PSCs and 2D layer $A_3B_2X_9$ PSCs to some extent, their efficiency is still much lower than that of lead-based perovskites. In this case, although dimensionality modulation does not fully address the limitations of $A_3B_2X_9$ to date, it can still be instructive in their future development.

4.2 Perovskite-like rudorffites

Inspired by perovskites, rudorffites are also considered potential candidates for photovoltaic application.[193,199,205,206] Rudorffites have the chemical formula of $Ag_xBi_yI_{x+3y}$ and their tunable compositions result in various symmetries, such as $R\bar{3}m$ for the Ag-rich compound and $Fd\bar{3}m$ for the Bi-rich counterpart.[191,207,208] However, despite the suitable direct bandgaps achieved in some compounds,[188,195,201,209] the current PCE of rudorffite solar cells[23,195] still falls short of the expectation (Table 4). This is primarily attributed to their poor carrier mobility[207,210] due to their low structure dimensionality, and consequently low electronic dimensionality.

In this case, dimensionality modulation *via* the adjustment of the ratio of the components is an effective way to enhance the performance of solar cells. A variation in the composition ratio between Ag and Bi leads to a change in the lattice symmetry, which affects its dimensionality. Furthermore, distinct characteristics such as mobility and electronic state density arise from the difference in the structures. In the case of the Ag-rich component with a layered structure (*e.g.*, Ag_3BiI_6, Fig. 27a), the occupation of additional Ag between layers leads to an enhancement in vertical charge transport across layers, and thus its electronic dimensionality.[211] In the case of the Bi-rich component (*e.g.*, $AgBi_2I_7$, Fig. 27b) in the cubic phase, it has a defect-spinel structure, where the tetrahedral sites are entirely vacant (Fig. 25b). With an increase in the Bi ratio, the number of vacant sites in rudorffites increases, resulting in poor carrier transport.[208] This difference is further proven by the carrier effective mass in the calculation of the band structures (Fig. 27c and d) and related carrier mobility.[210,212] The flexibility of dimensionality makes this category diverse and designable, suggesting its potential success in the future.

5. Conclusions and perspectives

In this review, we systematically reviewed the dimensionality modulation in different categories of lead-free perovskites and perovskite-like materials. Given that the limitations originate from either the octahedra distortion or the intrinsic low-dimensional structure, both structural and electronic dimensionality changes have a great effect on the optoelectronic properties in the corresponding solar cells. Future perspectives on the further development of lead-free perovskites and perovskite-inspired materials for photovoltaic applications can be summarized as follows:

(1) Considering the facile oxidation of tin(II) from a chemical perspective, it is essential to use reductive additives to passivate

Table 4 Summary of reported rudorffite solar cells based on different compositions

Category	Structure	Method	Bandgap (eV)	PCE (%)	Ref.
$AgBiI_4$	FTO/c-TiO_2/m-TiO_2/$AgBiI_4$/PTAA/Ag	Anti-solvent	1.86	2.10	186
	FTO/c-TiO_2/m-TiO_2/$AgBiI_4$/P3HT/Au	Thermal evaporation	1.86^{d}, 1.72^{in}	0.89	187
	ITO/SnO_2/$AgBiI_4$/PTAA/Au	Li-TFSI additive & anti-solvent	1.94^{d}, 1.79^{in}	2.80	188
	FTO/c-TiO_2/m-TiO_2/$AgBiI_4$/PTAA/Ag	Cs^+ doping & anti-solvent	1.95	1.58	189
	ITO/SnO_2/$AgBiI_4$/PTAA/Au	Anti-solvent	1.75^{d}	1.61	190
Ag_2BiI_5	FTO/c-TiO_2/m-TiO_2/Ag_2BiI_5/P3HT/Au	N_2 flow assisted	1.85^{d}, 1.62^{in}	2.10	191
	FTO/c-TiO_2/m-TiO_2/Ag_2BiI_5/spiro-OMeTAD/Au	Anti-solvent	1.83	1.74	192
	FTO/c-TiO_2/m-TiO_2/Ag_2BiI_5/spiro-OMeTAD/Ag	Solvent engineering	1.90^{d}	0.62	193
	ITO/SnO_2/Ag_2BiI_5/PTAA/Au	Compositional engineering & thickness optimization	1.90	1.13	194
Ag_3BiI_6	FTO/c-TiO_2/m-TiO_2/Ag_3BiI_6/PTAA/Au	Anti-solvent	1.83^{d}	4.30	23
	FTO/c-TiO_2/m-TiO_2/Ag_3BiI_6/PTAA/Au	S^{2-} doping & Ar flow assisted	1.84–1.89	5.56	195
	ITO/NiO_x/Ag_3BiI_6/PCBM/C_{60}/Au	Dynamic casting	1.88^{d}	1.08	196
	FTO/c-TiO_2/m-TiO_2/Ag_3BiI_6/P3HT/Au	Anti-solvent	1.80	2.32	197
	FTO/Sn:TiO_2/Ag_3BiI_6/PTAA/Au	Thermal-assisted doctor-blade coating	1.90	2.77	198
	FTO/c-TiO_2/m-TiO_2/m-ZrO_2/Ag_3BiI_6/C	CuSCN treatment	1.79^{d}	0.74	199
$AgBi_2I_7$	FTO/c-TiO_2/m-TiO_2/$AgBi_2I_7$/P3HT/Au	Normal spin-coating	1.87^{d}, 1.66^{in}	1.22	200
	FTO/c-TiO_2/m-TiO_2/$AgBi_2I_7$/spiro-OMeTAD/Au	HCl additive	1.93^{d}, 1.68^{in}	0.83	201
	FTO/c-TiO_2/m-TiO_2/$AgBi_2I_7$/P3HT/Au	Low temperature (90 °C) fabrication & anti-solvent	1.89^{d}, 1.78^{in}	2.12	202
	FTO/c-TiO_2/m-TiO_2/$AgBi_2I_7$/TQ_1/Au	Br^- doping	1.80^{d}, 1.63^{in}	1.02	203
$Ag_2Bi_3I_{11}$	FTO/c-TiO_2/m-TiO_2/$Ag_2Bi_3I_{11}$/spiro-OMeTAD/Au	Compositional engineering	1.81^{d}, 1.69^{in}	0.78	204

the grain boundaries in THPs. Further constructing LD/3D structures is a reliable way to simultaneously enhance the efficiency and stability of THPSCs. We note that the targeted introduction of appropriate spacers and modulation of the crystallization dynamics are strongly needed to obtain favorable heterogeneous microstructures, orientation, and *n*-value distributions for balanced overall device optimization. Also, by functionally tailoring the appropriate spacer cations, LD THPs with better intrinsic chemical stability can be obtained, inhibiting the oxidation reaction and generation of defects, as well as improving the band alignment.

(2) In the case of double perovskites, the main tasks are extending their absorption range and enhancing their carrier diffusion length. We welcome new ideas beyond the traditional three-dimensional double perovskites. Further efforts can be made to re-establish the connection of isolated band-edge-deriving octahedra, *e.g.* Ag and Bi octahedra in $Cs_2AgBiBr_6$, by specific atoms or molecules. Appropriate interstitial doping to enhance electronic dimensionality can be further studied. In addition, double perovskites and derivatives consisting of iodide and sulfur in a stable low-dimensional structure are proposed, such as quantum dots and quasi-2D materials.

(3) In the case of defect-structured materials with low-dimensional structures, the first thing is to minimize their defect density through vacancy passivation and edge stabilization. Further, it is essential to alleviate their low electronic dimensionality. They will benefit from either elemental doping for structural change or interstitial doping for electronic variation. Additionally, their carrier transport in vertical directions of PSCs can be further improved by rearranging the orientation of the low-dimensional structure, which is also significant for the current sandwich-structure PSCs.

(4) Finally, we propose the modification of the device structure for lead-free materials with low diffusion length, such as the mesoporous TiO_2 electron transport layer. In addition, co-deposition of lead-free materials with other organic or inorganic transport materials is another way to break the bottleneck of carrier extraction.

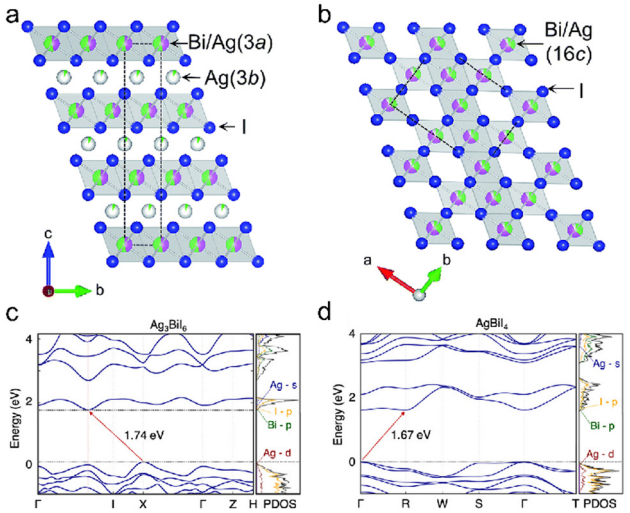

Fig. 27 Crystal structures of (a) Ag-rich rhombohedral phase and (b) Bi-rich cubic phase. The green, pink, and blue spheres represent Ag^+, Bi^{3+}, and I^- ions, respectively.[211] Reproduced from ref. 211 with permission from RSC Publishing, Copyright 2023. Band structures of (c) Ag_3BiI_6 and (d) $AgBiI_4$.[212] Reproduced from ref. 212 with permission from Wiley-VCH, Copyright 2022.

Author contributions

W. Yu and L. Xiao conceived the idea and constructed the review. W. Yu, Y. Zou and H. Wang conducted the literature search and wrote the manuscript. S. Qi, X. Guo and Y. Liu helped the literature search and manuscript writing. C. Wu, Z. Chen, and B. Qu helped to correct the manuscript. All the authors read, revised, and approved the final version.

Conflicts of interest

There are no conflicts to declare.

Acknowledgements

This study was financially supported by NSFC (No. 61935016, 52173153, 12174013 and 12074011).

References

1 W. Chen, Y. Zhu, J. Xiu, G. Chen, H. Liang, S. Liu, H. Xue, E. Birgersson, J. W. Ho, X. Qin, J. Lin, R. Ma, T. Liu, Y. He, A. M.-C. Ng, X. Guo, Z. He, H. Yan, A. B. Djurišić and Y. Hou, *Nat. Energy*, 2022, **7**, 229–237.
2 M. A. Green, E. D. Dunlop, M. Yoshita, N. Kopidakis, K. Bothe, G. Siefer and X. Hao, *Prog. Photovoltaics*, 2023, **31**, 651–663.
3 M. Jošt, E. Köhnen, A. Al-Ashouri, T. Bertram, Š. Tomšič, A. Magomedov, E. Kasparavicius, T. Kodalle, B. Lipovšek, V. Getautis, R. Schlatmann, C. A. Kaufmann, S. Albrecht and M. Topič, *ACS Energy Lett.*, 2022, **7**, 1298–1307.
4 R. Lin, J. Xu, M. Wei, Y. Wang, Z. Qin, Z. Liu, J. Wu, K. Xiao, B. Chen, S. M. Park, G. Chen, H. R. Atapattu, K. R. Graham, J. Xu, J. Zhu, L. Li, C. Zhang, E. H. Sargent and H. Tan, *Nature*, 2022, **603**, 73–78.
5 K. Xiao, Y.-H. Lin, M. Zhang, R. D. J. Oliver, X. Wang, Z. Liu, X. Luo, J. Li, D. Lai, H. Luo, R. Lin, J. Xu, Y. Hou, H. J. Snaith and H. Tan, *Science*, 2022, **376**, 762–767.
6 H. Dong, C. Ran, W. Gao, M. Li, Y. Xia and W. Huang, *eLight*, 2023, **3**, 3.
7 C. Ran, J. Xu, W. Gao, C. Huang and S. Dou, *Chem. Soc. Rev.*, 2018, **47**, 4581–4610.
8 H. Zhang, J.-W. Lee, G. Nasti, R. Handy, A. Abate, M. Grätzel and N.-G. Park, *Nature*, 2023, **617**, 687–695.
9 J. Li, J. Duan, X. Yang, Y. Duan, P. Yang and Q. Tang, *Nano Energy*, 2021, **80**, 105526.
10 M. Wang, W. Wang, B. Ma, W. Shen, L. Liu, K. Cao, S. Chen and W. Huang, *Nano-Micro Lett.*, 2021, **13**, 62.
11 T. Wu, X. Liu, X. Luo, X. Lin, D. Cui, Y. Wang, H. Segawa, Y. Zhang and L. Han, *Joule*, 2021, **5**, 863–886.
12 Z. Xiao, Z. Song and Y. Yan, *Adv. Mater.*, 2019, **31**, 1803792.
13 Y. Zhang, Y. Ma, Y. Wang, X. Zhang, C. Zuo, L. Shen and L. Ding, *Adv. Mater.*, 2021, **33**, 2006691.
14 J. Cao and F. Yan, *Energy Environ. Sci.*, 2021, **14**, 1286–1325.
15 T. Wu, Z. Qin, Y. Wang, Y. Wu, W. Chen, S. Zhang, M. Cai, S. Dai, J. Zhang, J. Liu, Z. Zhou, X. Liu, H. Segawa, H. Tan, Q. Tang, J. Fang, Y. Li, L. Ding, Z. Ning, Y. Qi, Y. Zhang and L. Han, *Nano-Micro Lett.*, 2021, **13**, 152.
16 F. Igbari, Z.-K. Wang and L.-S. Liao, *Adv. Energy Mater.*, 2019, **9**, 1803150.
17 W. Yu, Y. Zou, H. Wang, B. Qu, Z. Chen and L. Xiao, *J. Phys. Chem. Lett.*, 2023, **14**, 5310–5317.
18 M. Chen, M.-G. Ju, A. D. Carl, Y. Zong, R. L. Grimm, J. Gu, X. C. Zeng, Y. Zhou and N. P. Padture, *Joule*, 2018, **2**, 558–570.
19 R. Murshed, S. Thornton, C. Walkons, J. J. Koh and S. Bansal, *Sol. RRL*, 2023, 2300165.
20 F. Bai, Y. Hu, Y. Hu, T. Qiu, X. Miao and S. Zhang, *Sol. Energy Mater. Sol. Cells*, 2018, **184**, 15–21.
21 P. Karuppuswamy, K. M. Boopathi, A. Mohapatra, H.-C. Chen, K.-T. Wong, P.-C. Wang and C.-W. Chu, *Nano Energy*, 2018, **45**, 330–336.
22 G. Paul and A. J. Pal, *Sol. Energy*, 2022, **232**, 196–203.
23 I. Turkevych, S. Kazaoui, E. Ito, T. Urano, K. Yamada, H. Tomiyasu, H. Yamagishi, M. Kondo and S. Aramaki, *ChemSusChem*, 2017, **10**, 3754–3759.
24 O. Dupré, R. Vaillon and M. A. Green, *Sol. Energy Mater. Sol. Cells*, 2015, **140**, 92–100.
25 B.-B. Yu, Z. Chen, Y. Zhu, Y. Wang, B. Han, G. Chen, X. Zhang, Z. Du and Z. He, *Adv. Mater.*, 2021, **33**, 2102055.
26 M. Awais, R. L. Kirsch, V. Yeddu and M. I. Saidaminov, *ACS Mater. Lett.*, 2021, **3**, 299–307.
27 Y. J. Heo, H. J. Jang, J.-H. Lee, S. B. Jo, S. Kim, D. H. Ho, S. J. Kwon, K. Kim, I. Jeon, J.-M. Myoung, J. Y. Lee, J.-W. Lee and J. H. Cho, *Adv. Funct. Mater.*, 2021, **31**, 2106974.
28 A. Morteza Najarian, F. Dinic, H. Chen, R. Sabatini, C. Zheng, A. Lough, T. Maris, M. I. Saidaminov, F. P. García de Arquer, O. Voznyy, S. Hoogland and E. H. Sargent, *Nature*, 2023, **620**, 328–335.
29 A. D. Wright, L. R. V. Buizza, K. J. Savill, G. Longo, H. J. Snaith, M. B. Johnston and L. M. Herz, *J. Phys. Chem. Lett.*, 2021, **12**, 3352–3360.
30 Z. Xiao, W. Meng, J. Wang, D. B. Mitzi and Y. Yan, *Mater. Horiz.*, 2017, **4**, 206–216.
31 A. H. Slavney, T. Hu, A. M. Lindenberg and H. I. Karunadasa, *J. Am. Chem. Soc.*, 2016, **138**, 2138–2141.
32 C. Wu, Q. Zhang, Y. Liu, W. Luo, X. Guo, Z. Huang, H. Ting, W. Sun, X. Zhong, S. Wei, S. Wang, Z. Chen and L. Xiao, *Adv. Sci.*, 2018, **5**, 1700759.
33 Y. Zou, W. Yu, X. Li, H. Wang, B. Qu, Z. Chen and L. Xiao, *J. Phys. Chem. C*, 2023, **127**, 18301–18309.
34 W. Gao, C. Ran, J. Xi, B. Jiao, W. Zhang, M. Wu, X. Hou and Z. Wu, *Chem. Phys. Chem.*, 2018, **19**, 1696–1700.
35 A. J. Lehner, D. H. Fabini, H. A. Evans, C.-A. Hébert, S. R. Smock, J. Hu, H. Wang, J. W. Zwanziger, M. L. Chabinyc and R. Seshadri, *Chem. Mater.*, 2015, **27**, 7137–7148.
36 F. Umar, J. Zhang, Z. Jin, I. Muhammad, X. Yang, H. Deng, K. Jahangeer, Q. Hu, H. Song and J. Tang, *Adv. Opt. Mater.*, 2019, **7**, 1801368.
37 C. Wu, Q. Zhang, G. Liu, Z. Zhang, D. Wang, B. Qu, Z. Chen and L. Xiao, *Adv. Energy Mater.*, 2020, **10**, 1902496.
38 Q. Zhang, H. Ting, S. Wei, D. Huang, C. Wu, W. Sun, B. Qu, S. Wang, Z. Chen and L. Xiao, *Mater. Today Energy*, 2018, **8**, 157–165.
39 A. Chakraborty, N. Pai, J. Zhao, B. R. Tuttle, A. N. Simonov and V. Pecunia, *Adv. Funct. Mater.*, 2022, **32**, 2203300.
40 E. L. Lim, A. Hagfeldt and D. Bi, *Energy Environ. Sci.*, 2021, **14**, 3256–3300.
41 N. K. Noel, S. D. Stranks, A. Abate, C. Wehrenfennig, S. Guarnera, A.-A. Haghighirad, A. Sadhanala,

G. E. Eperon, S. K. Pathak, M. B. Johnston, A. Petrozza, L. M. Herz and H. J. Snaith, *Energy Environ. Sci.*, 2014, **7**, 3061–3068.
42 F. Hao, C. C. Stoumpos, D. H. Cao, R. P. H. Chang and M. G. Kanatzidis, *Nat. Photonics*, 2014, **8**, 489–494.
43 F. Hao, C. C. Stoumpos, P. Guo, N. Zhou, T. J. Marks, R. P. H. Chang and M. G. Kanatzidis, *J. Am. Chem. Soc.*, 2015, **137**, 11445–11452.
44 W. Liao, D. Zhao, Y. Yu, C. R. Grice, C. Wang, A. J. Cimaroli, P. Schulz, W. Meng, K. Zhu, R.-G. Xiong and Y. Yan, *Adv. Mater.*, 2016, **28**, 9333–9340.
45 S. Shao, J. Liu, G. Portale, H.-H. Fang, G. R. Blake, G. H. ten Brink, L. J. A. Koster and M. A. Loi, *Adv. Energy Mater.*, 2018, **8**, 1702019.
46 R. S. Drago, *J. Phys. Chem.*, 1958, **62**, 353–357.
47 P. Xu, S. Chen, H.-J. Xiang, X.-G. Gong and S.-H. Wei, *Chem. Mater.*, 2014, **26**, 6068–6072.
48 X. Jiang, Z. Zang, Y. Zhou, H. Li, Q. Wei and Z. Ning, *Acc. Mater. Res.*, 2021, **2**, 210–219.
49 J. Pascual, M. Flatken, R. Félix, G. Li, S.-H. Turren-Cruz, M. H. Aldamasy, C. Hartmann, M. Li, D. Di Girolamo, G. Nasti, E. Hüsam, R. G. Wilks, A. Dallmann, M. Bär, A. Hoell and A. Abate, *Angew. Chem., Int. Ed.*, 2021, **60**, 21583–21591.
50 M. E. Kayesh, K. Matsuishi, R. Kaneko, S. Kazaoui, J.-J. Lee, T. Noda and A. Islam, *ACS Energy Lett.*, 2019, **4**, 278–284.
51 G. Liu, C. Liu, Z. Lin, J. Yang, Z. Huang, L. Tan and Y. Chen, *ACS Appl. Mater. Interfaces*, 2020, **12**, 14049–14056.
52 X. Meng, J. Lin, X. Liu, X. He, Y. Wang, T. Noda, T. Wu, X. Yang and L. Han, *Adv. Mater.*, 2019, **31**, 1903721.
53 X. Meng, Y. Wang, J. Lin, X. Liu, X. He, J. Barbaud, T. Wu, T. Noda, X. Yang and L. Han, *Joule*, 2020, **4**, 902–912.
54 B. P. Nguyen, D. Shin, H. R. Jung, J. Kim, T. T. T. Nguyen, S. Yoon, Y. Yi and W. Jo, *Sol. Energy*, 2019, **186**, 136–144.
55 L. Rao, X. Meng, S. Xiao, Z. Xing, Q. Fu, H. Wang, C. Gong, T. Hu, X. Hu, R. Guo and Y. Chen, *Angew. Chem., Int. Ed.*, 2021, **60**, 14693–14700.
56 T. Wu, X. Liu, X. He, Y. Wang, X. Meng, T. Noda, X. Yang and L. Han, *Sci. China: Chem.*, 2020, **63**, 107–115.
57 Z. Zhu, X. Jiang, D. Yu, N. Yu, Z. Ning and Q. Mi, *ACS Energy Lett.*, 2022, **7**, 2079–2083.
58 F. Li, C. Zhang, J.-H. Huang, H. Fan, H. Wang, P. Wang, C. Zhan, C.-M. Liu, X. Li, L.-M. Yang, Y. Song and K.-J. Jiang, *Angew. Chem., Int. Ed.*, 2019, **58**, 6688–6692.
59 X. Meng, T. Wu, X. Liu, X. He, T. Noda, Y. Wang, H. Segawa and L. Han, *J. Phys. Chem. Lett.*, 2020, **11**, 2965–2971.
60 T.-B. Song, T. Yokoyama, S. Aramaki and M. G. Kanatzidis, *ACS Energy Lett.*, 2017, **2**, 897–903.
61 M. E. Kayesh, T. H. Chowdhury, K. Matsuishi, R. Kaneko, S. Kazaoui, J.-J. Lee, T. Noda and A. Islam, *ACS Energy Lett.*, 2018, **3**, 1584–1589.
62 C. Wang, F. Gu, Z. Zhao, H. Rao, Y. Qiu, Z. Cai, G. Zhan, X. Li, B. Sun, X. Yu, B. Zhao, Z. Liu, Z. Bian and C. Huang, *Adv. Mater.*, 2020, **32**, 1907623.
63 C. Wang, Y. Zhang, F. Gu, Z. Zhao, H. Li, H. Jiang, Z. Bian and Z. Liu, *Matter*, 2021, **4**, 709–721.
64 Q. Wei, Y. Ke and Z. Ning, *Energy Environ. Mater.*, 2020, **3**, 541–547.
65 Q. Tai, X. Guo, G. Tang, P. You, T.-W. Ng, D. Shen, J. Cao, C.-K. Liu, N. Wang, Y. Zhu, C.-S. Lee and F. Yan, *Angew. Chem., Int. Ed.*, 2019, **58**, 806–810.
66 M. I. Saidaminov, I. Spanopoulos, J. Abed, W. Ke, J. Wicks, M. G. Kanatzidis and E. H. Sargent, *ACS Energy Lett.*, 2020, **5**, 1153–1155.
67 R. Azmi, E. Ugur, A. Seitkhan, F. Aljamaan, A. S. Subbiah, J. Liu, G. T. Harrison, M. I. Nugraha, M. K. Eswaran, M. Babics, Y. Chen, F. Xu, T. G. Allen, A. U. Rehman, C.-L. Wang, T. D. Anthopoulos, U. Schwingenschlögl, M. De Bastiani, E. Aydin and S. De Wolf, *Science*, 2022, **376**, 73–77.
68 S. Sidhik, Y. Wang, M. De Siena, R. Asadpour, A. J. Torma, T. Terlier, K. Ho, W. Li, A. B. Puthirath, X. Shuai, A. Agrawal, B. Traore, M. Jones, R. Giridharagopal, P. M. Ajayan, J. Strzalka, D. S. Ginger, C. Katan, M. A. Alam, J. Even, M. G. Kanatzidis and A. D. Mohite, *Science*, 2022, **377**, 1425–1430.
69 S. Silver, Q. Dai, H. Li, J.-L. Brédas and A. Kahn, *Adv. Energy Mater.*, 2019, **9**, 1901005.
70 H. Tsai, W. Nie, J.-C. Blancon, C. C. Stoumpos, R. Asadpour, B. Harutyunyan, A. J. Neukirch, R. Verduzco, J. J. Crochet, S. Tretiak, L. Pedesseau, J. Even, M. A. Alam, G. Gupta, J. Lou, P. M. Ajayan, M. J. Bedzyk, M. G. Kanatzidis and A. D. Mohite, *Nature*, 2016, **536**, 312–316.
71 D. H. Cao, C. C. Stoumpos, T. Yokoyama, J. L. Logsdon, T.-B. Song, O. K. Farha, M. R. Wasielewski, J. T. Hupp and M. G. Kanatzidis, *ACS Energy Lett.*, 2017, **2**, 982–990.
72 Y. Liao, H. Liu, W. Zhou, D. Yang, Y. Shang, Z. Shi, B. Li, X. Jiang, L. Zhang, L. N. Quan, R. Quintero-Bermudez, B. R. Sutherland, Q. Mi, E. H. Sargent and Z. Ning, *J. Am. Chem. Soc.*, 2017, **139**, 6693–6699.
73 X. Jiang, H. Li, Q. Zhou, Q. Wei, M. Wei, L. Jiang, Z. Wang, Z. Peng, F. Wang, Z. Zang, K. Xu, Y. Hou, S. Teale, W. Zhou, R. Si, X. Gao, E. H. Sargent and Z. Ning, *J. Am. Chem. Soc.*, 2021, **143**, 10970–10976.
74 Z. Xing, Z. Zang, H. Li, Z. Ning, K. S. Wong and P. C. Y. Chow, *J. Phys. Chem. Lett.*, 2023, **14**, 4349–4356.
75 P. Li, X. Liu, Y. Zhang, C. Liang, G. Chen, F. Li, M. Su, G. Xing, X. Tao and Y. Song, *Angew. Chem., Int. Ed.*, 2020, **59**, 6909–6914.
76 J. Qiu, Y. Xia, Y. Zheng, W. Hui, H. Gu, W. Yuan, H. Yu, L. Chao, T. Niu, Y. Yang, X. Gao, Y. Chen and W. Huang, *ACS Energy Lett.*, 2019, **4**, 1513–1520.
77 S. Shao, J. Dong, H. Duim, G. H. ten Brink, G. R. Blake, G. Portale and M. A. Loi, *Nano Energy*, 2019, **60**, 810–816.
78 M. Liao, B.-B. Yu, Z. Jin, W. Chen, Y. Zhu, X. Zhang, W. Yao, T. Duan, I. Djerdj and Z. He, *ChemSusChem*, 2019, **12**, 5007–5014.
79 W.-G. Choi, C.-G. Park, Y. Kim and T. Moon, *ACS Energy Lett.*, 2020, **5**, 3461–3467.
80 K. Chen, P. Wu, W. Yang, R. Su, D. Luo, X. Yang, Y. Tu, R. Zhu and Q. Gong, *Nano Energy*, 2018, **49**, 411–418.

81 C. Ran, J. Xi, W. Gao, F. Yuan, T. Lei, B. Jiao, X. Hou and Z. Wu, *ACS Energy Lett.*, 2018, **3**, 713–721.
82 J. Li, P. Hu, Y. Chen, Y. Li and M. Wei, *ACS Sustainable Chem. Eng.*, 2020, **8**, 8624–8628.
83 M. Chen, Q. Dong, F. T. Eickemeyer, Y. Liu, Z. Dai, A. D. Carl, B. Bahrami, A. H. Chowdhury, R. L. Grimm, Y. Shi, Q. Qiao, S. M. Zakeeruddin, M. Grätzel and N. P. Padture, *ACS Energy Lett.*, 2020, **5**, 2223–2230.
84 M. Chen, M.-G. Ju, M. Hu, Z. Dai, Y. Hu, Y. Rong, H. Han, X. C. Zeng, Y. Zhou and N. P. Padture, *ACS Energy Lett.*, 2019, **4**, 276–277.
85 S. Cho, P. Pandey, J. Park, T.-W. Lee, H. Ahn, H. Choi and D.-W. Kang, *Chem. Eng. J.*, 2022, **446**, 137388.
86 W. Gao, C. Chen, C. Ran, H. Zheng, H. Dong, Y. Xia, Y. Chen and W. Huang, *Adv. Funct. Mater.*, 2020, **30**, 2000794.
87 W. Gu, X. Xu, J. Chen, B. Ma, M. Qin, W. Zhu, J. Qian, Z. Qin, W. Shen, Y. Lu, W. Zhang, S. Chen, X. Lu and W. Huang, *Sol. RRL*, 2020, **4**, 2000153.
88 P. Li, H. Dong, J. Xu, J. Chen, B. Jiao, X. Hou, J. Li and Z. Wu, *ACS Energy Lett.*, 2020, **5**, 2327–2334.
89 C. Ran, W. Gao, J. Li, J. Xi, L. Li, J. Dai, Y. Yang, X. Gao, H. Dong, B. Jiao, I. Spanopoulos, C. D. Malliakas, X. Hou, M. G. Kanatzidis and Z. Wu, *Joule*, 2019, **3**, 3072–3087.
90 K. Nishimura, M. A. Kamarudin, D. Hirotani, K. Hamada, Q. Shen, S. Iikubo, T. Minemoto, K. Yoshino and S. Hayase, *Nano Energy*, 2020, **74**, 104858.
91 E. Jokar, C.-H. Chien, C.-M. Tsai, A. Fathi and E. W.-G. Diau, *Adv. Mater.*, 2019, **31**, 1804835.
92 D. Cui, X. Liu, T. Wu, X. Lin, X. Luo, Y. Wu, H. Segawa, X. Yang, Y. Zhang, Y. Wang and L. Han, *Adv. Funct. Mater.*, 2021, **31**, 2100931.
93 Z. Zhang, Y. Huang, C. Wang, Y. Jiang, J. Jin, J. Xu, Z. Li, Z. Su, Q. Zhou, J. Zhu, R. He, D. Hou, H. Lai, S. Ren, C. Chen, X. Gao, T. Shi, W. Hu, F. Fu, P. Gao and D. Zhao, *Energy Environ. Sci.*, 2023, **16**, 3430–3440.
94 Y. Jiang, Z. Lu, S. Zou, H. Lai, Z. Zhang, J. Luo, Y. Huang, R. He, J. Jin, Z. Yi, Y. Luo, W. Wang, C. Wang, X. Hao, C. Chen, X. Wang, Y. Wang, S. Ren, T. Shi, F. Fu and D. Zhao, *Nano Energy*, 2022, **103**, 107818.
95 X. Liu, T. Wu, J.-Y. Chen, X. Meng, X. He, T. Noda, H. Chen, X. Yang, H. Segawa, Y. Wang and L. Han, *Energy Environ. Sci.*, 2020, **13**, 2896–2902.
96 T. Wu, D. Cui, X. Liu, X. Meng, Y. Wang, T. Noda, H. Segawa, X. Yang, Y. Zhang and L. Han, *Sol. RRL*, 2020, **4**, 2000240.
97 F. Li, J. Zhang, S. Jo, M. Qin, Z. Li, T. Liu, X. Lu, Z. Zhu and A. K. Y. Jen, *Small Methods*, 2020, **4**, 1900831.
98 H. Li, Z. Zang, Q. Wei, X. Jiang, M. Ma, Z. Xing, J. Wang, D. Yu, F. Wang, W. Zhou, K. S. Wong, P. C. Y. Chow, Y. Zhou and Z. Ning, *Sci. China: Chem.*, 2023, **66**, 459–465.
99 L. Wang, Q. Miao, D. Wang, M. Chen, H. Bi, J. Liu, A. K. Baranwal, G. Kapil, Y. Sanehira, T. Kitamura, T. Ma, Z. Zhang, Q. Shen and S. Hayase, *Angew. Chem., Int. Ed.*, 2023, **62**, e202307228.
100 J. Zhou, M. Hao, Y. Zhang, X. Ma, J. Dong, F. Lu, J. Wang, N. Wang and Y. Zhou, *Matter*, 2022, **5**, 683–693.
101 G. Liu, X. Jiang, W. Feng, G. Yang, X. Chen, Z. Ning and W.-Q. Wu, *Angew. Chem., Int. Ed.*, 2023, **62**, e202305551.
102 X. Jiang, Z. Zang, M. Ma, J. Wang, H. Wang and Z. Ning, *ACS Photonics*, 2023, **10**, 1992–1998.
103 V. M. Goldschmidt, *Ber. dtsch. Ber. Dtsch. Chem. Ges., Beil.*, 1927, **60**, 1263–1296.
104 C. Li, X. Lu, W. Ding, L. Feng, Y. Gao and Z. Guo, *Acta Crystallogr., Sect. B: Struct. Sci.*, 2008, **64**, 702–707.
105 J. I. Uribe, D. Ramirez, J. M. Osorio-Guillén, J. Osorio and F. Jaramillo, *J. Phys. Chem. C*, 2016, **120**, 16393–16398.
106 G. Kieslich, S. Sun and A. K. Cheetham, *Chem. Sci.*, 2014, **5**, 4712–4715.
107 B. Morosin and K. Emerson, *Acta Crystallogr., Sect. B: Struct. Crystallogr. Cryst. Chem.*, 1976, **32**, 294–295.
108 C. C. Stoumpos, L. Frazer, D. J. Clark, Y. S. Kim, S. H. Rhim, A. J. Freeman, J. B. Ketterson, J. I. Jang and M. G. Kanatzidis, *J. Am. Chem. Soc.*, 2015, **137**, 6804–6819.
109 F. Ji, G. Boschloo, F. Wang and F. Gao, *Sol. RRL*, 2023, **7**, 2201112.
110 W. Meng, X. Wang, Z. Xiao, J. Wang, D. B. Mitzi and Y. Yan, *J. Phys. Chem. Lett.*, 2017, **8**, 2999–3007.
111 D. J. Kubicki, M. Saski, S. MacPherson, K. Gałkowski, J. Lewiński, D. Prochowicz, J. J. Titman and S. D. Stranks, *Chem. Mater.*, 2020, **32**, 8129–8138.
112 E. T. McClure, M. R. Ball, W. Windl and P. M. Woodward, *Chem. Mater.*, 2016, **28**, 1348–1354.
113 F. Ji, Y. Huang, F. Wang, L. Kobera, F. Xie, J. Klarbring, S. Abbrent, J. Brus, C. Yin, S. I. Simak, I. A. Abrikosov, I. A. Buyanova, W. M. Chen and F. Gao, *Adv. Funct. Mater.*, 2020, **30**, 2005521.
114 G. Liu, Z. Zhang, C. Wu, Y. Zhang, X. Li, W. Yu, G. Yao, S. Liu, J.-J. Shi, K. Liu, Z. Chen, L. Xiao and B. Qu, *Adv. Funct. Mater.*, 2022, **32**, 2109891.
115 Z. Zhang, G. Liu, W. Guo, X. Li, Y. Zhang, C. Wu, B. Qu, J.-J. Shi, Z. Chen and L. Xiao, *Mater. Adv.*, 2022, **3**, 4932–4937.
116 Y. Jiao, S. Zhang, Z. Yang and G. Lu, *Comput. Theor. Chem.*, 2019, **1148**, 55–59.
117 F. Schmitz, J. Horn, N. Dengo, A. E. Sedykh, J. Becker, E. Maiworm, P. Bélteky, Á. Kukovecz, S. Gross, F. Lamberti, K. Müller-Buschbaum, D. Schlettwein, D. Meggiolaro, M. Righetto and T. Gatti, *Chem. Mater.*, 2021, **33**, 4688–4700.
118 B. A. Connor, L. Leppert, M. D. Smith, J. B. Neaton and H. I. Karunadasa, *J. Am. Chem. Soc.*, 2018, **140**, 5235–5240.
119 B.-H. Wang, B. Gao, J.-R. Zhang, L. Chen, G. Junkang, S. Shen, C.-T. Au, K. Li, M.-Q. Cai and S.-F. Yin, *Phys. Chem. Chem. Phys.*, 2021, **23**, 12439–12448.
120 M. K. Jana, S. M. Janke, D. J. Dirkes, S. Dovletgeldi, C. Liu, X. Qin, K. Gundogdu, W. You, V. Blum and D. B. Mitzi, *J. Am. Chem. Soc.*, 2019, **141**, 7955–7964.
121 P. Vishnoi, J. L. Zuo, X. Li, D. C. Binwal, K. E. Wyckoff, L. Mao, L. Kautzsch, G. Wu, S. D. Wilson, M. G. Kanatzidis, R. Seshadri and A. K. Cheetham, *J. Am. Chem. Soc.*, 2022, **144**, 6661–6666.
122 C. N. Savory, A. Walsh and D. O. Scanlon, *ACS Energy Lett.*, 2016, **1**, 949–955.

123 M. A. Hadi, M. N. Islam and J. Podder, *RSC Adv.*, 2022, **12**, 15461–15469.
124 F. Ji, J. Klarbring, F. Wang, W. Ning, L. Wang, C. Yin, J. S. M. Figueroa, C. K. Christensen, M. Etter, T. Ederth, L. Sun, S. I. Simak, I. A. Abrikosov and F. Gao, *Angew. Chem., Int. Ed.*, 2020, **59**, 15191–15194.
125 G. Ji, C. Han, S. Hu, P. Fu, X. Chen, J. Guo, J. Tang and Z. Xiao, *J. Am. Chem. Soc.*, 2021, **143**, 10275–10281.
126 X. Y. Qian, N. W. Cheung, M. A. Lieberman, M. I. Current, P. K. Chu, W. L. Harrington, C. W. Magee and E. M. Botnick, *Nucl. Instrum. Methods Phys. Res., Sect. B*, 1991, **55**, 821–825.
127 Z. Zhang, Q. Sun, Y. Lu, F. Lu, X. Mu, S.-H. Wei and M. Sui, *Nat. Commun.*, 2022, **13**, 3397.
128 Y. Liu, W. Gao, C. Ran, H. Dong, N. Sun, X. Ran, Y. Xia, L. Song, Y. Chen and W. Huang, *ChemSusChem*, 2020, **13**, 6477–6497.
129 J. Zhang, C. Yang, Y. L. Liao, S. J. Li, P. F. Yang, Y. X. Xi, W. G. Liu, D. A. Golosov, S. M. Zavadski and S. N. Melnikov, *Nanomaterials*, 2022, **12**, 2279.
130 X. Huang, S. Huang, P. Biswas and R. Mishra, *J. Phys. Chem. C*, 2016, **120**, 28924–28932.
131 S. Sun, S. Tominaka, J.-H. Lee, F. Xie, P. D. Bristowe and A. K. Cheetham, *APL Mater.*, 2016, **4**, 031101.
132 S. Nair, A. Bhorde, R. Kulkarni, B. Bade, A. Punde, P. Vairale, Y. Hase, A. Waghmare, R. Waykar, M. Deshpande, M. Prasad and S. Jadkar, *Mater. Today: Proc.*, 2021, **34**, 684–689.
133 S. Weber, T. Rath, K. Fellner, R. Fischer, R. Resel, B. Kunert, T. Dimopoulos, A. Steinegger and G. Trimmel, *ACS Appl. Energy Mater.*, 2019, **2**, 539–547.
134 K. Ahmad, P. Kumar, H. Kim and S. M. Mobin, *ChemNanoMat*, 2022, **8**, e202200061.
135 B.-B. Yu, M. Liao, J. Yang, W. Chen, Y. Zhu, X. Zhang, T. Duan, W. Yao, S.-H. Wei and Z. He, *J. Mater. Chem. A*, 2019, **7**, 8818–8825.
136 B.-W. Park, B. Philippe, X. Zhang, H. Rensmo, G. Boschloo and E. M. J. Johansson, *Adv. Mater.*, 2015, **27**, 6806–6813.
137 Z. Ma, S. Peng, Y. Wu, X. Fang, X. Chen, X. Jia, K. Zhang, N. Yuan, J. Ding and N. Dai, *Phys. B*, 2017, **526**, 136–142.
138 B. Ghosh, B. Wu, H. K. Mulmudi, C. Guet, K. Weber, T. C. Sum, S. Mhaisalkar and N. Mathews, *ACS Appl. Mater. Interfaces*, 2018, **10**, 35000–35007.
139 M. B. Johansson, B. Philippe, A. Banerjee, D. Phuyal, S. Mukherjee, S. Chakraborty, M. Cameau, H. Zhu, R. Ahuja, G. Boschloo, H. Rensmo and E. M. J. Johansson, *Inorg. Chem.*, 2019, **58**, 12040–12052.
140 R. Waykar, A. Bhorde, S. Nair, S. Pandharkar, B. Gabhale, R. Aher, S. Rondiya, A. Waghmare, V. Doiphode, A. Punde, P. Vairale, M. Prasad and S. Jadkar, *J. Phys. Chem. Solids*, 2020, **146**, 109608.
141 K. Ahmad, P. Kumar and S. M. Mobin, *Chem. – Asian J.*, 2020, **15**, 2859–2863.
142 S. M. Masawa, J. H. Li, C. X. Zhao, X. L. Liu and J. X. Yao, *Materials*, 2022, **15**, 2180.
143 K. Ahmad, M. Q. Khan, R. A. Khan and H. Kim, *Opt. Mater.*, 2022, **128**, 112458.
144 S. L. Hamukwaya, H. Y. Hao, M. M. Mashingaidze, T. T. Zhong, S. Tang, J. J. Dong, J. Xing and H. Liu, *Nanomaterials*, 2022, **12**, 3751.
145 W. Yuan, Y. Xu, T. Ding, Q. Wang, Z. Shao and M. Zhong, *Opt. Mater.*, 2023, **139**, 113815.
146 A. Dehingia, A. Shabir, U. Das, K. K. Borgohain, S. Patra, P. K. Sarkar, C. M. Tan and A. Roy, *ACS Appl. Electron. Mater.*, 2023, **5**, 5332–5342.
147 S. Vijaya, J. Subbiah, D. J. Jones and S. Anandan, *RSC Adv.*, 2023, **13**, 9978–9982.
148 X. Zhang, G. Wu, Z. Gu, B. Guo, W. Liu, S. Yang, T. Ye, C. Chen, W. Tu and H. Chen, *Nano Res.*, 2016, **9**, 2921–2930.
149 C. Ran, Z. Wu, J. Xi, F. Yuan, H. Dong, T. Lei, X. He and X. Hou, *J. Phys. Chem. Lett.*, 2017, **8**, 394–400.
150 S. S. Mali, H. Kim, D.-H. Kim and C. Kook Hong, *ChemistrySelect*, 2017, **2**, 1578–1585.
151 T. Okano and Y. Suzuki, *Mater. Lett.*, 2017, **191**, 77–79.
152 Z. Zhang, X. Li, X. Xia, Z. Wang, Z. Huang, B. Lei and Y. Gao, *J. Phys. Chem. Lett.*, 2017, **8**, 4300–4307.
153 J. Li, X. Liu, J. Xu, J. Chen, C. Zhao, M. Salma Maneno, B. Zhang and J. Yao, *Sol. RRL*, 2019, **3**, 1900218.
154 Y. Zhang, F. Fadaei Tirani, P. Pattison, K. Schenk-Joß, Z. Xiao, M. K. Nazeeruddin and P. Gao, *Dalton Trans.*, 2020, **49**, 5815–5822.
155 K. Ahmad, P. Kumar, P. Shrivastava and S. M. Mobin, *Energy Technol.*, 2022, **10**, 2100717.
156 J. Li, H. Han, B. Li, C. Zhao, J. Xu and J. Yao, *J. Alloys Compd.*, 2022, **909**, 164725.
157 K. Ahmad, M. Quasim Khan, A. Alsulmi and H. Kim, *Chem. – Eur. J.*, 2023, **29**, e202300513.
158 K. M. Boopathi, P. Karuppuswamy, A. Singh, C. Hanmandlu, L. Lin, S. A. Abbas, C. C. Chang, P. C. Wang, G. Li and C. W. Chu, *J. Mater. Chem. A*, 2017, **5**, 20843–20850.
159 J.-P. Correa-Baena, L. Nienhaus, R. C. Kurchin, S. S. Shin, S. Wieghold, N. T. Putri Hartono, M. Layurova, N. D. Klein, J. R. Poindexter, A. Polizzotti, S. Sun, M. G. Bawendi and T. Buonassisi, *Chem. Mater.*, 2018, **30**, 3734–3742.
160 A. Singh, S. Najman, A. Mohapatra, Y.-J. Lu, C. Hanmandlu, C.-W. Pao, Y.-F. Chen, C. S. Lai and C.-W. Chu, *ACS Appl. Mater. Interfaces*, 2020, **12**, 32649–32657.
161 A. Singh, P.-T. Lai, A. Mohapatra, C.-Y. Chen, H.-W. Lin, Y.-J. Lu and C. W. Chu, *Chem. Eng. J.*, 2021, **419**, 129424.
162 J. H. Li, Y. G. Lv, H. F. Han, J. Xu and J. X. Yao, *Materials*, 2022, **15**, 2883.
163 A. Hiltunen, N. Lamminen, H. Salonen, M. Liu and P. Vivo, *Sustainable Energy Fuels*, 2022, **6**, 217–222.
164 A. Singh, K. M. Boopathi, A. Mohapatra, Y. F. Chen, G. Li and C. W. Chu, *ACS Appl. Mater. Interfaces*, 2018, **10**, 2566–2573.
165 N. Lamminen, G. K. Grandhi, F. Fasulo, A. Hiltunen, H. Pasanen, M. Liu, B. Al-Anesi, A. Efimov, H. Ali-Löytty, K. Lahtonen, P. Mäkinen, A. Matuhina, A. B. Muñoz-García, M. Pavone and P. Vivo, *Adv. Energy Mater.*, 2023, **13**, 2203175.
166 Y. Zhang, F. Liu, H. Su, W. Yu, Y. Zou, C. Wu, X. Zhang, J. Zhang, Y. Liang, J. Han, Y. Guan, Y. Zhang, Z. Ye, R. Li, L. Xiao and S. Zheng, *Adv. Funct. Mater.*, 2023, 2304063.
167 Y. Guo, J. Zhou, F. Zhao, Y. Wu, J. Tao, S. Zuo, J. Jiang, Z. Hu and J. Chu, *Nano Energy*, 2021, **88**, 106281.

168 F. Zhao, J. Zhou, J. Tao, Y. Guo, J. Jiang and J. Chu, *J. Alloys Compd.*, 2022, **897**, 162741.
169 Y. Guo, F. Zhao, P. Yang, M. Gao, J. Shen, J. Tao, J. Jiang and J. Chu, *J. Mater. Chem. A*, 2023, **11**, 6474–6482.
170 C. Zuo and L. Ding, *Angew. Chem., Int. Ed.*, 2017, **56**, 6528–6532.
171 F. Jiang, D. Yang, Y. Jiang, T. Liu, X. Zhao, Y. Ming, B. Luo, F. Qin, J. Fan, H. Han, L. Zhang and Y. Zhou, *J. Am. Chem. Soc.*, 2018, **140**, 1019–1027.
172 S. Chatterjee and A. J. Pal, *ACS Appl. Mater. Interfaces*, 2018, **10**, 35194–35205.
173 Y. Yang, C. Liu, M. Cai, Y. Liao, Y. Ding, S. Ma, X. Liu, M. Guli, S. Dai and M. K. Nazeeruddin, *ACS Appl. Mater. Interfaces*, 2020, **12**, 17062–17069.
174 N. Giesbrecht, A. Weis and T. Bein, *JPhys Energy*, 2020, **2**, 024007.
175 Y. Zhang, J. Yin, M. R. Parida, G. H. Ahmed, J. Pan, O. M. Bakr, J.-L. Brédas and O. F. Mohammed, *J. Phys. Chem. Lett.*, 2017, **8**, 3173–3177.
176 K.-H. Hong, J. Kim, L. Debbichi, H. Kim and S. H. Im, *J. Phys. Chem. C*, 2017, **121**, 969–974.
177 B. Ghosh, S. Chakraborty, H. Wei, C. Guet, S. Li, S. Mhaisalkar and N. Mathews, *J. Phys. Chem. C*, 2017, **121**, 17062–17067.
178 M. Pazoki, M. B. Johansson, H. Zhu, P. Broqvist, T. Edvinsson, G. Boschloo and E. M. J. Johansson, *J. Phys. Chem. C*, 2016, **120**, 29039–29046.
179 K. M. McCall, Z. Liu, G. Trimarchi, C. C. Stoumpos, W. Lin, Y. He, I. Hadar, M. G. Kanatzidis and B. W. Wessels, *ACS Photonics*, 2018, **5**, 3748–3762.
180 M. B. Johansson, H. Zhu and E. M. J. Johansson, *J. Phys. Chem. Lett.*, 2016, **7**, 3467–3471.
181 J. Shin, M. Kim, S. Jung, C. S. Kim, J. Park, A. Song, K.-B. Chung, S.-H. Jin, J. H. Lee and M. Song, *Nano Res.*, 2018, **11**, 6283–6293.
182 H. Tang, K. J. Yuan, P. F. Zheng, T. Q. Xiao, H. W. Zhang, X. C. Zhao, W. Zhou, S. Y. Wang and W. F. Liu, *J. Solid State Chem.*, 2023, **323**, 124011.
183 H. Dammak, A. Yangui, S. Triki, Y. Abid and H. Feki, *J. Lumin.*, 2015, **161**, 214–220.
184 B. Saparov, F. Hong, J.-P. Sun, H.-S. Duan, W. Meng, S. Cameron, I. G. Hill, Y. Yan and D. B. Mitzi, *Chem. Mater.*, 2015, **27**, 5622–5632.
185 G. Tang, Z. Xiao, H. Hosono, T. Kamiya, D. Fang and J. Hong, *J. Phys. Chem. Lett.*, 2018, **9**, 43–48.
186 C. Lu, J. Zhang, H. Sun, D. Hou, X. Gan, M.-H. Shang, Y. Li, Z. Hu, Y. Zhu and L. Han, *ACS Appl. Energy Mater.*, 2018, **1**, 4485–4492.
187 M. Khazaee, K. Sardashti, C.-C. Chung, J.-P. Sun, H. Zhou, E. Bergmann, W. A. Dunlap-Shohl, Q. Han, I. G. Hill and J. L. Jones, *J. Mater. Chem. A*, 2019, **7**, 2095–2105.
188 Q. Zhang, C. Wu, X. Qi, F. Lv, Z. Zhang, Y. Liu, S. Wang, B. Qu, Z. Chen and L. Xiao, *ACS Appl. Energy Mater.*, 2019, **2**, 3651–3656.
189 F. Yu, L. Wang, K. Ren, S. Yang, Z. Xu, Q. Han and T. Ma, *ACS Sustainable Chem. Eng.*, 2020, **8**, 9980–9987.
190 W. Zhai, L. Huang, X. Cui, G. Li, Z. Zhang, P. Chen, Y. Li, Y. Tang, L. Lin and Z. Yan, *J. Mater. Chem. C*, 2022, **10**, 5321–5327.
191 H. Zhu, M. Pan, M. B. Johansson and E. M. J. Johansson, *ChemSusChem*, 2017, **10**, 2592–2596.
192 K. W. Jung, M. R. Sohn, H. M. Lee, I. S. Yang, S. Do Sung, J. Kim, E. W.-G. Diau and W. I. Lee, *Sustainable Energy Fuels*, 2018, **2**, 294–302.
193 M. S. Shadabroo, H. Abdizadeh, M. Shabani and M. R. Golobostanfard, *Inorg. Chem.*, 2021, **60**, 11110–11119.
194 N. B. Correa Guerrero, Z. Guo, N. Shibayama, A. K. Jena and T. Miyasaka, *ACS Appl. Energy Mater.*, 2023, **6**, 10274–10284.
195 N. Pai, J. Lu, T. R. Gengenbach, A. Seeber, A. S. R. Chesman, L. Jiang, D. C. Senevirathna, P. C. Andrews, U. Bach, Y.-B. Cheng and A. N. Simonov, *Adv. Energy Mater.*, 2019, **9**, 1803396.
196 Y. Seo, S. R. Ha, S. Yoon, S. M. Jeong, H. Choi and D.-W. Kang, *J. Power Sources*, 2020, **453**, 227903.
197 A. Kulkarni, F. Ünlü, N. Pant, J. Kaur, C. Bohr, A. K. Jena, S. Öz, M. Yanagida, Y. Shirai and M. Ikegami, *Sol. RRL*, 2021, **5**, 2100077.
198 K.-C. Hsiao, Y.-F. Yu, C.-M. Ho, M.-H. Jao, Y.-H. Chang, S.-H. Chen, Y.-H. Chang, W.-F. Su, K.-M. Lee and M.-C. Wu, *Chem. Eng. J.*, 2023, **451**, 138807.
199 Y. Yuan and N. Robertson, *Sustainable Energy Fuels*, 2023, **7**, 1067–1076.
200 Y. Kim, Z. Yang, A. Jain, O. Voznyy, G. H. Kim, M. Liu, L. N. Quan, F. P. García de Arquer, R. Comin and J. Z. Fan, *Angew. Chem., Int. Ed.*, 2016, **55**, 9586–9590.
201 Z. Shao, T. Le Mercier, M. B. Madec and T. Pauporté, *Mater. Lett.*, 2018, **221**, 135–138.
202 A. Kulkarni, A. K. Jena, M. Ikegami and T. Miyasaka, *Chem. Commun.*, 2019, **55**, 4031–4034.
203 H. Wu, H. Zhu, A. Erbing, M. B. Johansson, S. Mukherjee, G. J. Man, H. Rensmo, M. Odelius and E. M. Johansson, *ACS Appl. Energy Mater.*, 2019, **2**, 5356–5362.
204 Z. Shao, T. Le Mercier, M. Madec and T. Pauporte, *Mater. Des.*, 2018, **141**, 81–87.
205 T.-G. Kwon, T. Kim and Y. Kim, *Electron. Mater. Lett.*, 2023, DOI: **10.1007/s13391-023-00437-0**.
206 Y. Wang, Y. Liu, X. Shi, L. Huang, J. Tong, G. Wang and D. Pan, *New J. Chem.*, 2021, **45**, 14158–14166.
207 V. Pecunia, Y. Yuan, J. Zhao, K. Xia, Y. Wang, S. Duhm, L. Portilla and F. Li, *Nano-Micro Lett.*, 2020, **12**, 27.
208 Z. Shao, T. Le Mercier, M. B. Madec and T. Pauporté, *Mater. Des.*, 2018, **141**, 81–87.
209 M. D. Prasad, M. G. Krishna and S. K. Batabyal, *ACS Appl. Mater. Interfaces*, 2021, **4**, 1252–1259.
210 B. Ghosh, B. Wu, X. Guo, P. C. Harikesh, R. A. John, T. Baikie, Arramel, A. T. S. Wee, C. Guet, T. C. Sum, S. Mhaisalkar and N. Mathews, *Adv. Energy Mater.*, 2018, **8**, 1802051.
211 A. Koedtruad, M. Goto, M. Amano Patino, Z. Tan, H. Guo, T. Nakamura, T. Handa, W.-T. Chen, Y.-C. Chuang, H.-S. Sheu, T. Saito, D. Kan, Y. Kanemitsu, A. Wakamiya and Y. Shimakawa, *J. Mater. Chem. A*, 2019, **7**, 5583–5588.
212 B. Cucco, L. Pedesseau, C. Katan, J. Even, M. Kepenekian and G. Volonakis, *Sol. RRL*, 2022, **6**, 2200718.

